

# Non-linear MHD modelling of edge localized modes suppression by resonant magnetic perturbations in ITER

**Citation for published version (APA):**

Becoulet, M., Huijsmans, G. T. A., Passeron, C., Liu, Y. Q., Evans, T. E., Lao, L. L., Li, L., Loarte, A., Pinches, S. D., Polevoi, A., Hosokawa, M., Kim, S. K., Pamela, S. J. P., & Futatani, S. (2022). Non-linear MHD modelling of edge localized modes suppression by resonant magnetic perturbations in ITER. *Nuclear Fusion*, 62(6), Article 066022. <https://doi.org/10.1088/1741-4326/ac47af>

**Document license:**  
TAVERNE

**DOI:**  
[10.1088/1741-4326/ac47af](https://doi.org/10.1088/1741-4326/ac47af)

**Document status and date:**  
Published: 01/06/2022

**Document Version:**  
Publisher's PDF, also known as Version of Record (includes final page, issue and volume numbers)

**Please check the document version of this publication:**

- A submitted manuscript is the version of the article upon submission and before peer-review. There can be important differences between the submitted version and the official published version of record. People interested in the research are advised to contact the author for the final version of the publication, or visit the DOI to the publisher's website.
- The final author version and the galley proof are versions of the publication after peer review.
- The final published version features the final layout of the paper including the volume, issue and page numbers.

[Link to publication](#)

**General rights**

Copyright and moral rights for the publications made accessible in the public portal are retained by the authors and/or other copyright owners and it is a condition of accessing publications that users recognise and abide by the legal requirements associated with these rights.

- Users may download and print one copy of any publication from the public portal for the purpose of private study or research.
- You may not further distribute the material or use it for any profit-making activity or commercial gain
- You may freely distribute the URL identifying the publication in the public portal.

If the publication is distributed under the terms of Article 25fa of the Dutch Copyright Act, indicated by the "Taverne" license above, please follow below link for the End User Agreement:

[www.tue.nl/taverne](http://www.tue.nl/taverne)

**Take down policy**

If you believe that this document breaches copyright please contact us at:

[openaccess@tue.nl](mailto:openaccess@tue.nl)

providing details and we will investigate your claim.

PAPER

# Non-linear MHD modelling of edge localized modes suppression by resonant magnetic perturbations in ITER







To cite this article: M. Becoulet *et al* 2022 *Nucl. Fusion* **62** 066022

View the [article online](#) for updates and enhancements.

## You may also like

- [Enhancements of residual Reynolds stresses by magnetic perturbations in the edge plasmas of the J-TEXT tokamak](#)  
K.J. Zhao, Z.P. Chen, Yuejiang Shi et al.
- [Direct effects of the resonant magnetic perturbation on turbulent transport](#)  
M. Vlad and F. Spineanu
- [Resonant magnetic perturbation-mediated nonlinear interaction and its impact on magnetic field stochastization in pedestal collapse simulations](#)  
Juhyung Kim, S.S. Kim and Hogun Jhang

# Non-linear MHD modelling of edge localized modes suppression by resonant magnetic perturbations in ITER

M. Becoulet<sup>1,\*</sup>, G.T.A. Huijsmans<sup>1,2</sup>, C. Passeron<sup>1</sup>, Y.Q. Liu<sup>3</sup>, T.E. Evans<sup>3,a</sup>, L.L. Lao<sup>3</sup>, L. Li<sup>4</sup>, A. Loarte<sup>5</sup>, S.D. Pinches<sup>5</sup>, A. Polevoi<sup>5</sup>, M. Hosokawa<sup>5</sup>, S.K. Kim<sup>6</sup>, S.J.P. Pamela<sup>7</sup>, S. Futatani<sup>8</sup> and the JOEUK Team<sup>b</sup>

<sup>1</sup> CEA, IRFM, 13108 Saint-Paul-Lez-Durance, France

<sup>2</sup> Eindhoven University of Technology, PO Box 513, Eindhoven 5600 MB, The Netherlands

<sup>3</sup> General Atomics, PO Box 85608, San Diego, CA 92186-5608, United States of America

<sup>4</sup> Donghua University, 1882 Yan'an Road West, Shanghai, 200051, China

<sup>5</sup> ITER Organization, Route de Vinon-sur-Verdon, 13067 St Paul Lez Durance, France

<sup>6</sup> Princeton Plasma Physics Laboratory, PO Box 451, Princeton, NJ 08540, United States of America

<sup>7</sup> CCFE, Culham Science Centre, Oxon, OX14 3DB, UK Abingdon, United Kingdom of Great Britain and Northern Ireland

<sup>8</sup> Universitat Politècnica de Catalunya, Barcelona, Spain

E-mail: [marina.becoulet@cea.fr](mailto:marina.becoulet@cea.fr)

Received 3 June 2021, revised 10 November 2021

Accepted for publication 4 January 2022

Published 5 April 2022



CrossMark

## Abstract

Edge localized modes (ELMs) suppression by resonant magnetic perturbations (RMPs) was studied with the non-linear magneto-hydro-dynamic (MHD) code JOEUK for the ITER H-mode scenarios at 15 MA, 12.5 MA, 10 MA/5.3 T. The main aim of this work was to demonstrate that ELMs can be suppressed by RMPs while the divertor 3D footprints of heat and particle fluxes remain within divertor material limits. The unstable peeling–ballooning modes responsible for ELMs without RMPs were modelled first for each scenario using numerically accessible parameters for ITER. Then the stabilization of ELMs by RMPs was modelled with the same parameters. RMP spectra, optimized by the linear MHD MARS-F code, with main toroidal harmonics  $N = 2$ ,  $N = 3$ ,  $N = 4$  have been used as boundary conditions of the computational domain of JOEUK, including realistic RMP coils, main plasma, scrape off layer (SOL) divertor and realistic first wall. The model includes all relevant plasma flows: toroidal rotation, two fluid diamagnetic effects and neoclassical poloidal friction. With RMPs, the main toroidal harmonic and the non-linearly coupled harmonics remain dominant at the plasma edge, producing saturated modes and a continuous MHD turbulent transport thereby avoiding ELM crashes in all scenarios considered here. The threshold for ELM suppression was found at a maximum RMP coils current of 45 kAt–60 kAt compared to the coils maximum capability of 90 kAt. In the high beta poloidal steady-state 10 MA/5.3 T scenario, a rotating QH-mode without ELMs was observed even without RMPs. In this scenario with RMPs  $N = 3$ ,  $N = 4$  at 20 kAt maximum current in RMP coils, similar QH-mode behaviour was observed however with dominant edge harmonic corresponding to the main toroidal number of RMPs. The present MHD modelling was limited in time by few tens of ms after RMPs were switched on until the magnetic energy of the modes saturates.

\* Author to whom any correspondence should be addressed.

<sup>a</sup> Deceased.

<sup>b</sup> See Hoelzl *et al* 2021 (*Nucl. Fusion* in preparation) for the JOEUK Team.

As a consequence the thermal energy was still evolving on this time scale, far from the ITER confinement time scale and hence only the form of 3D footprints on the divertor targets can be indicated within this set-up. Also note, that the divertor physics was missing in this model, so realistic values of fluxes are out of reach in this modelling. However the stationary 3D divertor and particle fluxes could be simply extrapolated from these results to the stationary situation considering that a large power fraction should be radiated in the core and SOL and only about 50 MW power is going to the divertor, which is an arbitrary, but reasonable number used here. The 3D footprints with RMPs show the characteristic splitting with the main RMP toroidal symmetry. The maximum radial extension of the footprints typically was  $\sim 20$  cm in inner divertor and  $\sim 40$  cm in outer divertor with stationary heat fluxes decreasing further out from the initial strike point from  $\sim 5$  MW m $^{-2}$  to  $\sim 1$  MW m $^{-2}$  assuming a total power in the divertor and walls is 50 MW. The heat fluxes remain within the divertor target and baffle areas, however with rather small margin in the outer divertor which could be an issue for the first wall especially in transient regimes when part of the plasma thermal energy is released due to switching on the RMP coils. This fact should be considered when RMPs are applied with a more favorable application before or soon after the L–H transition, although optimization is required to avoid increasing the L–H power threshold with RMPs.

Keywords: ELM, RMP, ITER, MHD, JOEKE

(Some figures may appear in colour only in the online journal)

## 1. Introduction

The aim of the ITER project is the demonstration of the scientific feasibility of a nuclear fusion reactor based on a magnetic confinement concept as a future source of energy [1, 2]. The large increase of the plasma energy with the size of the machine leads to large steady-state heat fluxes on plasma facing components (PFCs). The ITER divertor is designed to handle these large stationary heat fluxes up to  $\sim 10$  MW m $^{-2}$  [1, 2]. However, magneto-hydro-dynamic (MHD) instabilities in tokamak plasmas can lead to transient bursts of heat fluxes of much larger amplitude than the steady-state fluxes. Edge localised modes (ELMs), driven by the pressure gradient and/or the current flowing in the plasma, are typical for the high confinement (H-mode) scenario in tokamaks [2, 3]. ELMs generate a perturbation of the structure of the magnetic field leading to quasi-periodic transient energy losses on a few hundred microseconds time scale [3, 4]. Each ELM can release up to 5%–10% of the thermal pedestal plasma energy [2] which, when scaled to ITER, represent 10–20 MJ and would result in transient large heat fluxes of several GW/m $^2$ , leading to an enhanced erosion of PFC and potentially representing an issue for the ITER divertor lifetime [1, 2]. This means that ELMs in ITER need to be controlled, either mitigated by limiting their amplitude or by completely stabilizing the ELM instability.

At present, the intensive experimental and theoretical study of ELM physics is particularly oriented towards finding and optimizing the methods of ELM control which can be used in ITER [1]. With this respect, the application of small resonant magnetic perturbations (RMPs) generated by specific coils demonstrated the possibility of total ELM suppression or strong mitigation of their size [2–10], motivating the use

of such method in ITER [1]. The initial understanding of the effect of RMPs on edge plasma and ELMs, based essentially on vacuum modelling results, suggested that, at certain level of external magnetic perturbation generated by the coils, the edge magnetic topology is perturbed forming overlapping islands and stochastic region where the heat and particle transport could be increased, lowering the pressure gradient and hence removing the main drive for ELMs. This empirical criterion combined with vacuum field modelling (without plasma response) was developed initially using DIII-D data [5] and suggested that ELMs are suppressed when the edge plasma is ergodized in the pedestal region (Chirikov parameter  $> 1$ ) for  $r/a > \sim 0.9$ . However the vacuum criterion has shown correlation with ELM suppression on some devices, but not on all of them. Note that this vacuum criterion was also used for the actual design the RMP in-vessel coils for ITER [13–15].

However, further experimental and theoretical studies, accomplished in the last decade, demonstrated that depending on the plasma parameters and on the RMP spectrum, the actual RMP field could be very different as compared to vacuum modelling results [16–22]. ELMs interaction with RMPs demonstrated a large variety of responses from no effect on ELMs, mitigation of ELM size or total ELM suppression for the same level of ergodization predicted by the vacuum modelling. Experimental, theoretical and modelling studies of the plasma response to RMPs were carried out leading to significant progress in the understanding of RMP physics [16–22], though many open questions still remain at present.

A comprehensive review of different models of the plasma response to the RMP fields is proposed in [21]. The most generic feature of the plasma response to RMPs is linked to

the plasma rotation, consisting that the generation of current perturbations near the rational surfaces can lead either to effective screening of RMPs [18], significantly reducing RMPs in plasma, or on the contrary at some specific conditions amplifying RMPs through external kink plasma response at the plasma edge [21, 22]. A key factor for RMPs screening proposed by reduced two-fluid MHD theory used in this paper is the electron velocity perpendicular to the magnetic field, including  $E \times B$  and diamagnetic drift which are usually large (few tens  $\text{km s}^{-1}$ ) in the pedestal region because of steep pressure and radial electric field gradients [18]. However the response currents in rotating plasmas are reduced at larger resistivity [18, 23] even at relatively strong perpendicular electron velocity in the pedestal region and, as a consequence, screening of RMPs decreases towards the plasma edge due to the temperature dependence  $\sim T_e^{(-3/2)}$  of the resistivity. Hence, at the very edge of the plasma the stochastization of the magnetic field usually happens with RMPs as observed in experiments [11].

It is known from experiment [5–12, 24] that RMPs can significantly influence both poloidal and toroidal rotations. For example, the poloidal plasma velocity responsible for RMP screening, is usually reduced starting from the certain threshold of the RMP current [25, 26]. This local braking of the electron poloidal rotation facilitates the RMP penetration into the pedestal region [26].

In addition in many experimental cases, the slowing down of the global toroidal rotation is also observed which was attributed to the neoclassical toroidal viscosity (NTV) mechanism [24, 27, 28]. NTV is resulting from the toroidal drag force experienced by the plasma particles moving along the field lines distorted by helical magnetic perturbations which affects both particle and toroidal torque transport. This global plasma braking can be an issue in using RMPs and in particular for core MHD modes locking and even disruptions [7]. On the other hand, in slow rotating plasmas as it is expected in ITER, NTV mechanism can be used to generate plasma rotation [24, 28].

The phenomenon of density ‘pump-out’ typically seen with RMP application is also far from being fully understood. The possible candidates as  $E \times B$  convective transport [26], NTV particle drift [22], polarization current [29] and increased turbulence with RMPs [30] were proposed by theory and modelling, but for the moment there is no global approach combining all these mechanisms which possibly all play a role in density ‘pump-out’.

Considering that the physics of RMPs is still far from being fully understood, the most important question however remains at what conditions ELMs are suppressed in present day machines and will they be suppressed in ITER scenarios? Recent modelling results of RMP experiments in ASDEX-Upgrade [26] and KSTAR [31] validated many aspects of the RMPs and ELMs physics models implemented in the non-linear resistive MHD JOREK code that we also used to model ELM suppression in ITER in this paper. It was demonstrated previously [19, 26, 31] that the non-linear multi-harmonics MHD approach, including a realistic tokamak geometry with

the X-point and the scrape-off-layer (SOL), realistic geometry and spectrum of RMP coils, toroidal rotation, bi-fluid diamagnetic effects and neoclassical poloidal friction represent a minimum model which permits to reproduce experimental results of ELM suppression in modelling. As it was shown in [19, 26, 31] RMPs drive non-linearly coupled side harmonics  $k \times N$  locked to the static RMP with main toroidal number  $N$  in the ELM suppression stage while strongly mitigating other harmonics responsible for ELM crash. It was shown that ELM are suppressed not only because of the reduction of the pressure gradient resulting from the heat and particle transport due to RMPs, but mainly due to these continuous MHD transport generated non-linearly [19, 26].

Recently a new ELM suppression criterion with plasma response based on the extensive comparison of ELM suppression experiments with ideal [22] and linear resistive MHD [21] pointed out that the external kink-peeling plasma response (maximum magnetic displacement near the X-point) is an important factor for ELM suppression and that the RMP spectrum should be adjusted with this respect. It was shown [21, 22] that the kink-peeling response is due to the special alignment of the RMP fields with respect to the plasma field and can be obtained in certain safety factor ( $q95$ ) window or adjusting the phasing between RMP coils at fixed  $q$ -profile. The criterion including the plasma response [21] provides an accurate alternative to predict ELM suppression in existing machines compared to vacuum criterion [5]. The ELM suppression with kink response with the optimal phasing of RMP coils was confirmed also in the non-linear MHD modelling [26]. However the non-linear MHD codes are too computer time consuming to be used for the optimization of the RMP spectrum. In this work we adapted a strategy to do optimization of RMP spectrum using linear MHD MARS-F code to satisfy the kink plasma response criterion and then to model ELMs suppression by RMPs with this optimized RMP spectrum, using non-linear code JOREK.

Another important consequence of RMP application is the complex magnetic topology at the edge and formation of a 3D SOL which lead to the splitting of the separatrix into a set of stable and unstable manifolds (homoclinic tangles) seen in experiment as helical ‘lobes’ at the X-point [11]. This results in the formation of non-axisymmetric heat and particle fluxes on the divertor target plates where helical finger-like structures or ‘footprints’ were observed in many RMP experiments [32–36]. The ITER divertor design [37] was done with the approximation of toroidal axisymmetry, but the 3D SOL transport and the plasma fluxes with RMPs will be very different and potentially can represent an issue, for example leading to local high heat fluxes (‘hot spots’) in the unprotected areas, additional fatigue stress in the divertor components and 3D material erosion of the divertor surface. Slow (few Hz) rotation of the RMP field is thus being considered as an option to spread out heat and particle fluxes [2]. However another issue can appear since such rotation of the RMP pattern can lead to large variations  $s$  of the coil current amplitudes and hence large mechanical stress in the RMP coils. The assessment of divertor heat and particle with RMPs in ITER represents a significant challenge since it demands both

self-consistent modelling of RMPs including non-linear MHD plasma response, full 3D fluid edge plasma (pedestal and SOL) transport including kinetic neutral transport, radiation, recycling, etc, what we will call here ‘divertor physics’. At present such numerical tools which include all relevant physics are not available for such a task. The estimation of the impact of RMPs on the stationary divertor heat and particle fluxes in ITER was done recently in [38], where the 3D plasma fluid and kinetic neutral transport code EMC3-EIRENE was used with the 3D magnetic structure including plasma response modelled with the linear resistive MHD code MARS-F. Such approach is a significant advance in the domain, but still has obvious limitations since the plasma response to RMPs was linear and was not non-self-consistently evolved. In the present work, we adopted the different strategy to model RMPs using the 3D non-linear resistive MHD code JOEAK which allows to calculate ELMs and RMP with self-consistent plasma response while taking into account two fluid diamagnetic effects, neo-classical poloidal friction and toroidal rotation in realistic ITER geometry including X-point, SOL and divertor. The model has previously been tested and validated on AUG and KSTAR RMP experiments [26, 31]. Such approach gives a more correct magnetic 3D topology and edge transport due to RMPs. However other limitations exist in this approach. The present MHD modelling was limited in time by few tens of ms after RMPs were switched on until the magnetic energy of the modes saturates. As a consequence the thermal energy was still evolving on this time scale, far from the ITER confinement time scale and hence only the form and position of 3D footprints on the divertor targets can be calculated within this set-up, but not the actual values of the stationary heat and particle fluxes. The realistic values of the stationary divertor fluxes with RMPs are out of reach in this modelling also because many aspects of the divertor physics are not yet included here compared to [38]. The 3D divertor heat and particle fluxes in the stationary RMP phase however could be extrapolated from these results to the stationary situation considering that a large power fraction should be radiated in the core and SOL and only 50 MW power is going to the divertor, which is an arbitrary, but reasonable number here.

Because of the present numerical limits of the code the numerically accessible ‘state of art’ parameters were used for ITER. Most importantly, the resistivity used to model the unstable peeling–ballooning modes responsible for ELMs was two orders of magnitude higher compared to Spitzer [39] resistivity. The stabilization of ELMs by RMPs was demonstrated in modelling using exactly the same parameters. For smaller machines like ASDEX-U a realistic resistivity was used in the simulation of ELM cycles using the JOEAK code [40]. However, for an ITER size machine the ‘state of art’ is still the use of larger resistivity and viscosity because of the numerical limits such as size of the grid, number of harmonics, numerical stability, HPC memory and available HPC time. Note also that Spitzer expression for the without kinetic effects is hardly applicable in ITER since the size of resistive layers is too small in ITER and compatible with ion Larmor radius, so kinetic effects should be taken into account which is not the case here. Another approach used for example in

the BOUT++ code for ELMs modelling at low actual Spitzer physical resistivity relies on use of ‘hyper-resistivity’ [41] to mimic dissipative small-scale electron turbulence. However it is also a model with its own numerical limits and the ELM size depends on the value of the chosen hyper-resistivity. The presented here results should be considered as a ‘state of art’ and a step forward. In the future more efforts will be needed to model ITER realistic parameters with further developments of the code JOEAK, but especially of future HPCs to overcome existing at present memory and time limits.

To summarize, the main concern of this work was to demonstrate that ELMs can be suppressed by RMPs while the divertor 3D footprints of heat and particle fluxes remain within divertor material limits.

The paper is organized as follows:

In section 2, a brief description of the model, boundary conditions, the construction of the flux-aligned mesh extended to the ITER divertor and the first wall, choice of numerical parameters and plasma profiles in the equilibrium with flows are presented for the ITER scenarios considered here. The RMP coils geometry and phasing between coils obtained by the MARS-F code providing maximum kink response are presented for all scenarios.

In section 3, the non-linear multi-harmonics modelling of natural ELMs without RMPs are presented in 15 MA and 12.5 MA scenarios. In the high beta 10 MA/5.3 T steady-state scenario, rotating natural QH-mode with low  $N$ -s edge harmonic oscillations was obtained.

In section 4, the modelling of ELMs with RMPs  $N = 2, 3, 4$  in the ITER 15 MA/5.3 T  $Q = 10$  scenario is described including a demonstration of the threshold for ELMs suppression by RMPs at about 45–60 kAt maximum current in RMP coils and the edge magnetic topology for each case considered here.

In section 5, the modelling of the interaction of RMPs with ELMs in 12.5/5.3 T  $Q = 5$  long pulse and 10 MA/5.3 T  $Q = 5$  steady-state scenarios are described.

In section 6, the magnetic surface displacement obtained by the linear MHD MARS-F and non-linear JOEAK codes are compared showing a good agreement but only at the early close to linear stage of RMP penetration obtained by the JOEAK code. In section 7, the heat and particle fluxes in divertor are presented for all scenarios with corresponding RMPs described above. The section 8, summarizes the work and presents the conclusions.

## 2. Model and initial conditions

### 2.1. Model, grid, boundary conditions

In the present work the 3D non-linear resistive MHD code JOEAK [42, 43] was used taking into account two fluid (for electrons and ions) diamagnetic effects, neo-classical poloidal friction and toroidal rotation in realistic ITER geometry including X-point, SOL and divertor and realistic RMP coils geometry and spectrum. The reduced MHD model was previously described and validated in modelling of ELM suppression experiments using RMPs in AUG [26] and KSTAR [31].

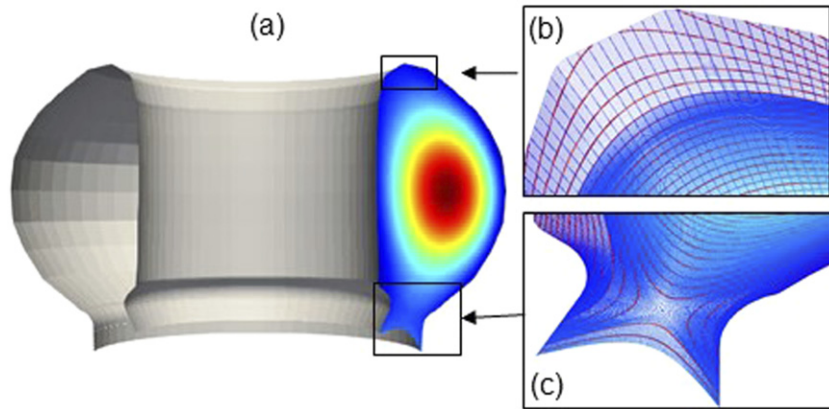


**Figure 1.** The extended to the wall JOREK grid used for modelling of the 15 MA/5.3 T scenario—(a), zoom at the top of the grid—(b) and in the X-point area—(c) with  $N_{\text{flux}} = 111$ -in radial direction and  $N_{\text{pol}} = 250$ -in poloidal direction. The ITER wall position is indicated by black points in (b) and (c).

**Table 1.** RMP coils phasing for different ITER scenarios used in modelling.

Scenario	IMAS reference	$N$	$\Delta\Phi_{\text{MARS}}^{\text{up}}$	$\Delta\Phi_{\text{MARS}}^{\text{mid}}$	$\Delta\Phi_{\text{MARS}}^{\text{low}}$	$\Delta\Phi_{\text{ERGOS}}^{\text{up}}$	$\Delta\Phi_{\text{ERGOS}}^{\text{mid}}$	$\Delta\Phi_{\text{ERGOS}}^{\text{low}}$
15 MA, Vtor(2)	131025_24	$N = 2$	$145^\circ$	$0^\circ$	$195^\circ$	$110.8^\circ$	$0^\circ$	$85.8^\circ$
		$N = 3$	$200^\circ$	$0^\circ$	$140^\circ$	$56.63^\circ$	$0^\circ$	$76.63^\circ$
		$N = 4$	$250^\circ$	$0^\circ$	$95^\circ$	$30.8^\circ$	$0^\circ$	$69.55^\circ$
15 MA, Vtor(1)	131025_23	$N = 3$	$200^\circ$	$0^\circ$	$140^\circ$	$56.63^\circ$	$0^\circ$	$76.63^\circ$
12.5 MA optimum	131039_0	$N = 3$	$215^\circ$	$0^\circ$	$120^\circ$	$51.63^\circ$	$0^\circ$	$83.3^\circ$
12.5 MA non-optimum	131039_0	$N = 3$	$135^\circ$	$0^\circ$	$25^\circ$	$78.3^\circ$	$0^\circ$	$114.97^\circ$
10 MA	131036_21	$N = 3$	$240^\circ$	$0^\circ$	$110^\circ$	$43.3^\circ$	$0^\circ$	$86.63^\circ$

In particular it was shown that toroidal plasma rotation and two fluid diamagnetic effects are essential to describe the non-linear RMP physics such as the evolution of plasma profiles, including radial electric field, screening of RMPs by plasma rotation, amplification of RMPs by the external kink plasma response and the interaction of ELMs with RMPs including ELMs suppression [26, 31]. The detailed description of JOREK code, boundary conditions and normalization including benchmarking with other codes and the examples of the validation for ELMs and RMP modelling can be found in [43]. Isoparametric cubic Bezier finite elements were used to construct a 2D grid in the poloidal cross-section [42, 43]. The continuity of all variables and their derivatives is satisfied on this  $C^1$  grid. The finite element grid is aligned to equilibrium flux surfaces for the three regions of the core, the SOL and the private region. The grid in the poloidal cross-section can be extended to the wall and actual divertor shape as it was the case here for ITER actual geometry. The example of the grid used for 15 MA/5.3 T scenario is presented in figure 1 where the mesh is locally more dense in the pedestal region with resolution  $N_{\text{flux}} = 111$ -in radial direction and  $N_{\text{pol}} = 250$ -in poloidal direction. The toroidal dimension is represented by a Fourier series. The time stepping is done using the implicit Crank–Nicolson or Gears scheme. The resulting sparse system of equations is solved using a generalized minimal residual solver with the preconditioner obtained by solving independently each sub-matrix corresponding to non-coupled Fourier

harmonics. These sub-matrices are solved using the direct parallel sparse matrix solver PaStiX (see [42, 43] and references therein). The boundary of the computational domain is limited by the ITER wall and divertor target plates. The boundary conditions around the computational domain correspond to those of an ideally conducting wall, where the magnetic and electric potential perturbations are set to zero. In the divertor and walls where the magnetic field lines cross the boundary, Bohm sheath boundary conditions were applied for the fluid velocity  $\vec{v}$ :

$$\frac{1}{|B|} \vec{B} \cdot \vec{v} = \pm C_s. \quad (1.1)$$

The heat flux is considered to be sheath limited at the targets and walls with a heat transmission factor as introduced in [44] with typical values for equal electron and ion temperatures:  $T_i = T_{e,\gamma_{\text{sh}}} \approx 8$ :

$$-K_{\parallel} \nabla_{\parallel} T \cdot \vec{n} = (\gamma_{\text{sh}}^{\text{jorek}} - 1) \cdot n_e \cdot T \cdot \vec{v}_{\parallel} \cdot \vec{n}. \quad (1.2)$$

Considering that total temperature is  $T = 2T_e$  and that  $V^2 = C_s^2 = \gamma k_B T / m_i$ , then the relation is following:  $\gamma_{\text{sh}}^{\text{jorek}} = (\gamma - 1)(0.5\gamma_{\text{sh}} - 0.5\gamma - 1)$ , where  $C_s = \sqrt{\gamma T / m_i}$  is ion sound speed,  $\gamma = \frac{5}{3}$ ,  $n_e$ —electron density,  $\vec{n}$ —is the unit vector normal to the divertor/wall surfaces. Here the value  $\gamma_{\text{sh}}^{\text{jorek}} \approx 2$  was used. The parallel thermal conductivity was flux-limited and is introduced in the following way. The total heat flux can

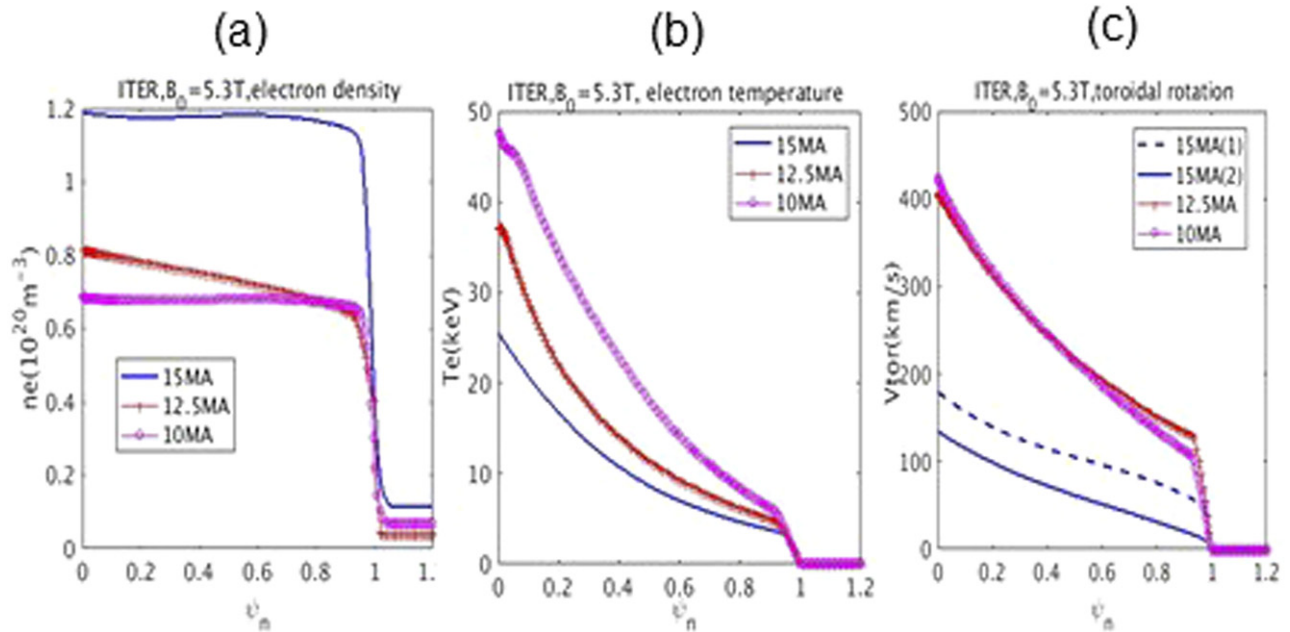


**Figure 2.** Initial electron density—(a), electron temperature—(b) and rotation profiles—(c) used in modelling for different ITER scenarios. Note that for 15 MA/5.3 T scenario two rotation profiles were used.

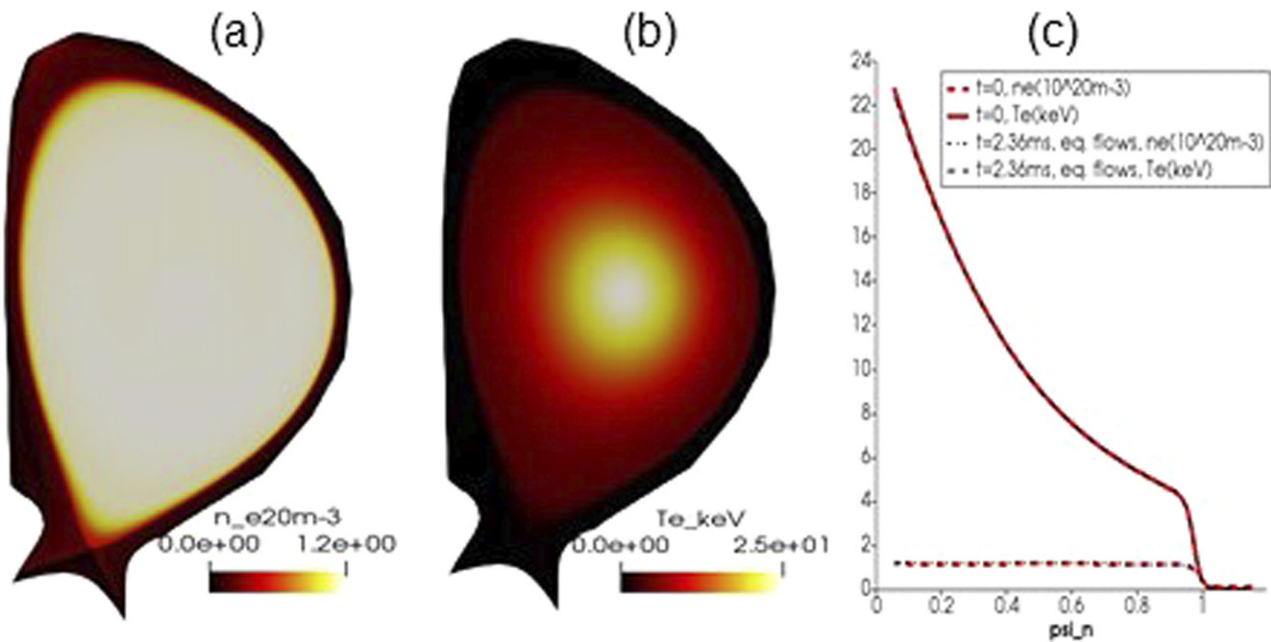


**Figure 3.** Equilibrium with flows for  $N = 0$  harmonic obtained in JOEJ for 15 MA scenario: (a)—electron density, (b)—electron temperature, (c)—comparison of initial (ASTRA) plasma profiles and plasma profiles in equilibrium with flows in JOEJ, which are identical.

be written as follows:

$$\vec{\Gamma} = -\chi_{\parallel} n_e \nabla_{\parallel} T_e - \chi_{\perp} n_e \nabla_{\perp} T_e + \frac{1}{(\gamma - 1)} \vec{V}(n_e T_e). \quad (1.3)$$

The Spitzer–Härm expression for thermal conductivity [45] implicitly assumes strongly collisional plasmas meaning that  $\lambda_{ee[m]} = 1.73 \cdot 10^{17} T_{e[eV]}^2 / (n_{e[m^{-3}} \ln \Lambda)$ —the electron mean free path is much shorter than the typical parallel scale length  $\lambda_{ee[m]} \ll L_T$  which can be taken as field line length

$L_T \approx \pi R q$ , where  $R$ —is major radius and  $q$ —is safety factor, here we take  $\ln \Lambda \approx 17$ . The plasma collisionality  $\nu^* = L_T / \lambda_{ee}$  varies strongly in the pedestal region and in particular  $\nu^* \ll 1$  at the top of the pedestal in H-mode scenarios in ITER. The Spitzer–Härm expression for thermal conductivity as it is given in [45] as following:

$$\Gamma_{\parallel [W m^{-2}]}^{\text{Spitzer}} = -\kappa_{\parallel [m^{-1} s^{-1}]}^{\text{Spitzer}} \frac{dT_{e[eV]}}{dI_{\parallel [m]}}, \quad (1.4)$$



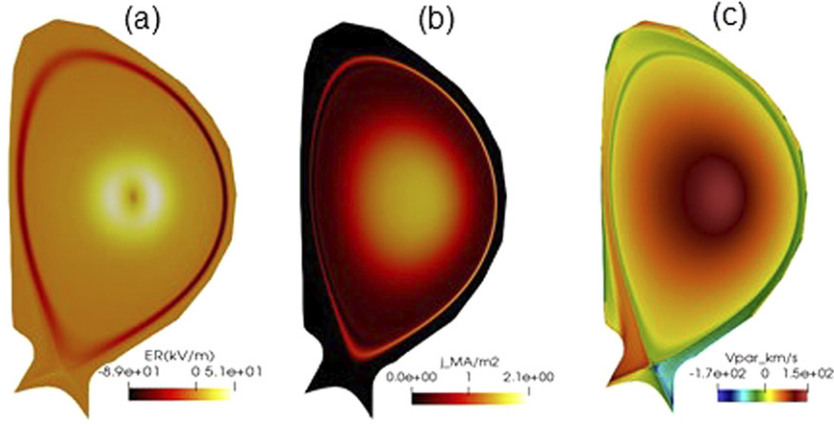


**Figure 4.** Equilibrium with flows for  $N = 0$  harmonic obtained in JOREK for 15 MA scenario: (a)—radial electric field (note the characteristic ‘well’ in the pedestal region), (b)—toroidal current including bootstrap at the plasma edge, (c)—established parallel velocity with Bohm boundary conditions at the magnetic field lines crossing divertor/walls.

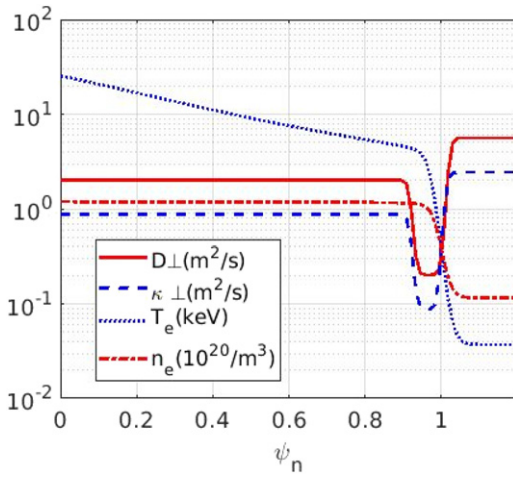


**Figure 5.** The perpendicular heat and particle conductivities chosen for modelling to keep electron density and temperature profiles close to the initial H-mode profiles in 15 MA scenario.

where  $\kappa_{\parallel}^{\text{Spitzer}} \approx 1.6 \cdot 10^{19} n_{e[m^{-3}]} V_{T_e[m s^{-1}]} \lambda_{ee[m]} = \chi_{\parallel[m^2 s^{-1}]}^{\text{Spitzer}} \cdot n_{e[m^{-3}]}$  and  $\frac{dT_e}{d\parallel} \sim \frac{T_e}{L_T}$  is a derivative of electron temperature along the magnetic field line,  $V_{T_e[m s^{-1}]}$  is thermal electron velocity

$$\chi_{\parallel[m^2 s^{-1}]}^{\text{Spitzer}} = 1.14 \cdot 10^{22} \frac{T_{e[eV]}^{5/2}}{n_{e[m^{-3}]}}, \quad (1.5)$$

For the low collisionality plasmas expression (1.5) lead to unphysical large heat fluxes even at very small parallel gradients, hence the kinetic approach is more appropriate in this case [44]. In order to extend the fluid approach to low collisionality plasmas the flux limit (FL) approximation was proposed in a number of papers [44, 46, 47] considering that:

$$\frac{1}{\Gamma_{\parallel}} = \frac{1}{\Gamma_{\parallel, \text{limit}}} + \frac{1}{\Gamma_{\parallel, \text{Spitzer}}}, \quad (1.6)$$

where  $\Gamma_{\parallel, \text{limit}[W m^{-2}]} = \alpha(1.6 \cdot 10^{19} n_{e[m^{-3}]} V_{T_e[m s^{-1}]} T_{e[eV]})$  and  $\alpha$  is an ad hoc numerical factor which in some cases can

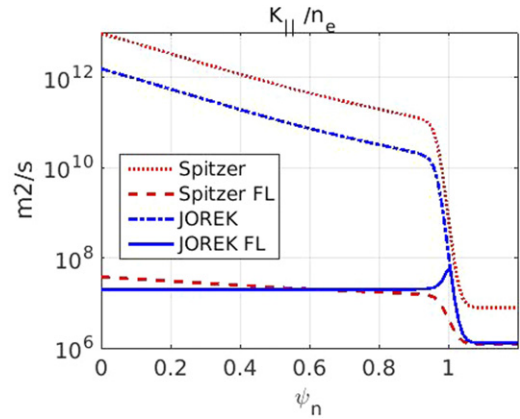


**Figure 6.** The parallel heat conductivity used in modelling (JOREK) is compared to Spitzer heat conductivity (Spitzer) with FL approximation. Note that in the JOREK code the parallel heat conductivity is simply limited by a constant in the core plasma which corresponds approximately to a FL (1.7).

be found from kinetic modelling if it exists and can vary significantly depending of the problem. Here we will use flux-limit approach for the central plasma as in [47] with  $\alpha = 3 \cdot 10^{-3}$ . The flux-limited expression for heat conductivity is the following:

$$\chi_{\parallel, \text{FL}} = \frac{\chi_{\parallel}^{\text{Spitzer}}}{1 + \lambda_{ee}/(\alpha L_T)}. \quad (1.7)$$

In this paper we were using equal temperatures for electron and ions which is usually the case in high density plasmas as in ITER, which permit to reduce number of variables, but in principle the temperatures can be different in the JOREK code [48]. Note also that the electron heat conductivity expression was used, however the heat conductivities are different for electrons and ions and this effect should be assessed in the future. Note however that here we used the two fluid version of JOREK which is needed to represent correctly rotation of ballooning modes responsible for ELMs [49] and screening of RMPs [18, 19, 26, 31].

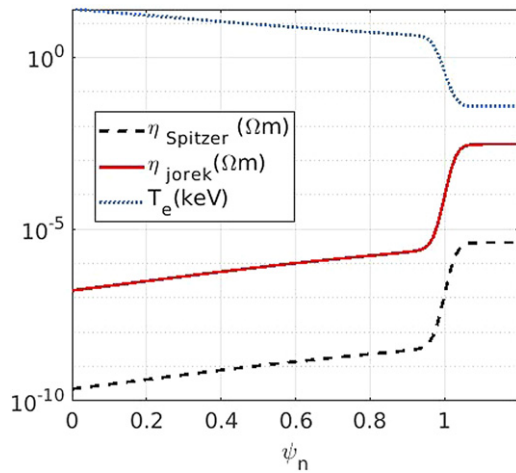


**Figure 7.** Spitzer resistivity, JOREK numerical resistivity and temperature profiles in 15 MA scenario.

## 2.2. Initial parameters, equilibrium with flows

The parameters of ITER H-mode scenarios with a magnetic field  $B_{\text{tor}} = 5.3$  T and plasma currents of 15 MA ( $Q = 10$  inductive), 12.5 MA ( $Q = 5$  long pulse) and 10 MA ( $Q = 5$  steady-state) as modelled by the ASTRA code [50] with toroidal flow profiles self-consistently calculated with NBI heating and momentum input, documented in ITER IMAS database (table 1) were used as initial conditions. The initial profiles are presented in figure 2. At the first step ( $t = 0$ ) the initial equilibrium is recalculated by JOREK on a polar mesh solving the Grad–Shafranov equation with the magnetic poloidal flux values at the boundary of the polar mesh taken from the IMAS ITER database, consistent with initial kinetic ASTRA profiles. Then a finite element grid is constructed which is aligned to the equilibrium flux surfaces in the core and the near SOL for better reproduction of the parallel transport. Then the grid is extended to follow the actual shape of ITER wall and divertor (figure 1).

On this grid the axi-symmetric stationary state with flows, the so-called ‘equilibrium with flows’, was calculated with the JOREK code evolving only one toroidal harmonic  $N = 0$  in time. All variables including magnetic flux, density, temperature, parallel flows, perpendicular velocities, radial electric field are established self-consistently taking into account boundary conditions, heating, momentum and particle sources and sinks. Similar procedures to obtain equilibrium with flows were done for 15 MA, 12.5 MA and 10 MA/5.3 T scenarios. As an example, we present the plasma parameters in the equilibrium with flows established after time  $\sim 2.36$  ms while only  $N = 0$  harmonic was evolving for 15 MA/5.3 T scenario (figures 3 and 4). The mid-plane profiles are presented in figure 3(c) in comparison with ASTRA profiles given as input at time  $t = 0$  showing that they are the same in the plasma core. To keep plasma profiles in the equilibrium with flows close to the initial profiles the perpendicular heat and particle conductivities were chosen as it shown in figure 5. The central value for perpendicular heat

conductivity is  $\sim 0.9$   $\text{m}^2 \text{s}^{-1}$  and for the perpendicular particle diffusivity  $\sim 1.3$   $\text{m}^2 \text{s}^{-1}$ , then both were decreased in the pedestal region (to  $\sim 0.09$   $\text{m}^2 \text{s}^{-1}$  for heat and to  $\sim 0.13$   $\text{m}^2 \text{s}^{-1}$  for particles diffusion respectively) to keep the H-mode profiles. The parallel heat conductivity used in the modelling is compared to Spitzer heat conductivity with FL approximation in figure 6. Note that in the JOREK code the parallel heat conductivity is simply limited by a constant in the core plasma which corresponds approximately to a FL (1.7). The parallel viscosity was constant in modelling which for numerical reasons taken here  $\mu_{\parallel,0} = 13$   $\text{m}^2 \text{s}^{-1}$  and the central value of the perpendicular viscosity was  $\mu_{\perp,0} = 1.3$   $\text{m}^2 \text{s}^{-1}$  with a temperature dependence used in JOREK  $\mu_{\perp} = \mu_{\perp,0}(T_e/T_{e,0})^{-3/2}$ . Neoclassical poloidal friction is taken constant for simplicity as in [18, 49] providing ion poloidal velocity close to the neoclassical value in the pedestal. The Spitzer resistivity calculated as in [39]  $\eta_{\parallel[\Omega m]} = 1.69 \cdot 10^{-9} \cdot \ln \Lambda \cdot T_{e[\text{keV}]}^{-3/2}$  and the one used in JOREK are presented in figure 7. Note that here we present parameters used in JOREK in SI for better understanding and comparison. The normalization of all parameters can be found in [43]. The resistivity used here was two orders higher compared to Spitzer resistivity (figure 7) due to the present numerical limits of the code JOREK for an ITER size machine, and existing limits of HPC memory and available computing time, as discussed in the introduction. The results presented here should be considered as a ‘state of art’ where we chose numerically accessible parameters for ITER to model firstly the unstable ballooning–peeling modes with a limited (due to HPC time and memory limits) number of toroidal harmonics and the full non-linear ELM crash due to them and then proceed with modelling of RMPs with exactly the same number harmonics and parameters to keep the underlying physics similar to previous studies for smaller machines [26, 31]. The aim of this work was to demonstrate that these modes responsible for the ELM crash can be stabilized by RMPs at certain RMP spectrum and current threshold in different ITER scenarios and at the same time have reasonable 3D divertor footprints with respect to the material limits. However note, that in the future more efforts will be needed to model ITER realistic parameters and divertor physics with further developments of the code JOREK, but especially of future HPCs to overcome existing at present memory and time limits.

## 2.3. Resonant magnetic perturbations

The vacuum RMPs generated by external coils were calculated by the vacuum code ERGOS [28] and are imposed at the computational boundary of the JOREK code, progressively increasing on a time scale of a few ms [18]. In the vacuum code ERGOS the horizontal parts of the RMP coils are approximated with curves and vertically with straight lines. The upper (1) and lower (2) corners of the coils were taken as follows: *upper row*:  $R_1 = 7.73$  m,  $Z_1 = 3.38$  m,  $R_2 = 8.26$  m,  $Z_2 = 2.62$  m; *middle*:  $R_1 = 8.62$  m,  $Z_1 = 1.79$  m,  $R_2 = 8.66$  m,  $Z_2 = -0.55$  m; *low*:  $R_1 = 8.23$  m,  $Z_1 = -1.55$  m,  $R_2 = 7.77$  m,  $Z_2 = -2.38$  m. The toroidal coordinates of the corners (the same for 1 and 2)

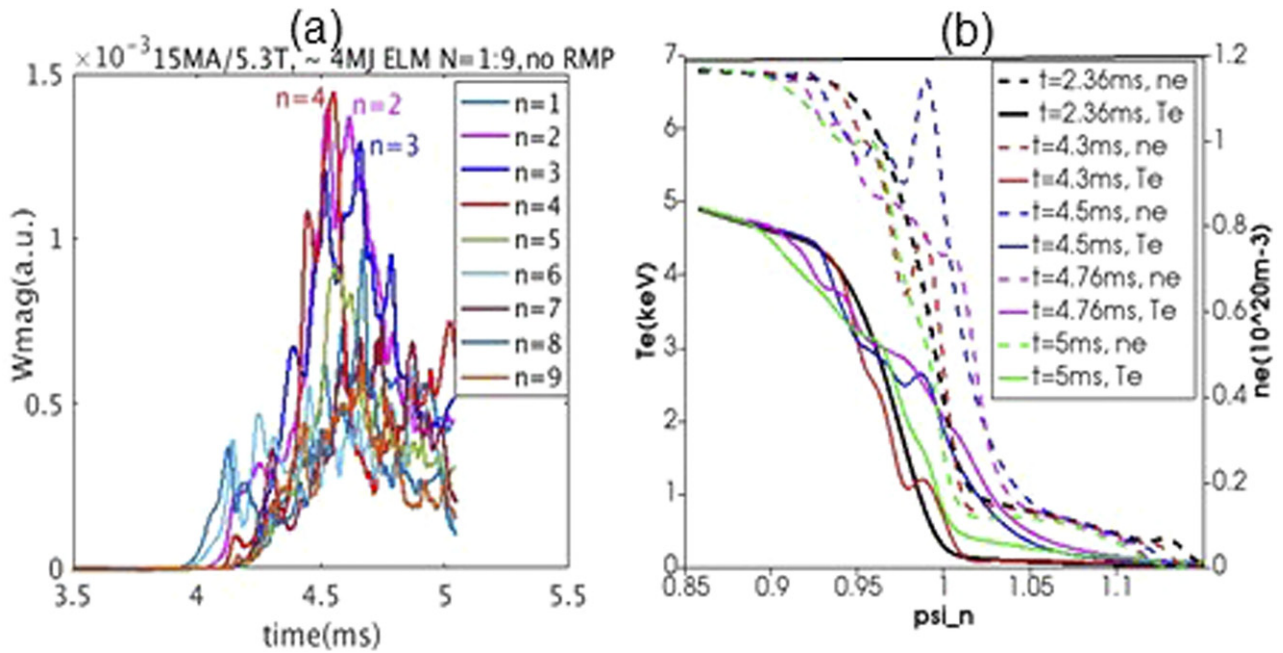


**Figure 8.** Magnetic energy in natural ELM with  $N = 1:9$  harmonics without RMPs in 15 MA scenario—(a) and changing electron temperature (in keV) and electron density (in  $10^{20} \text{ m}^{-3}$ ) profiles during ELM crash—(b).

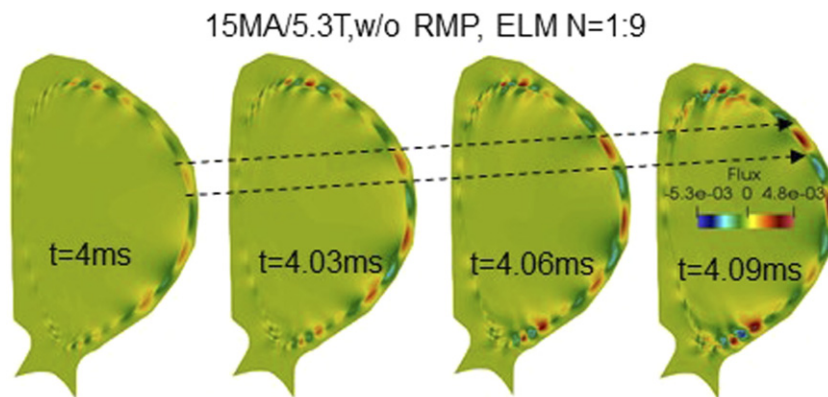


**Figure 9.** Modes  $N = 1:9$  rotation before ELM crash for 15 MA scenario.

of the nine coils in each row are calculated as following:  
 $\varphi_i^{(1)} = \Delta\varphi_{\text{width}}^{\text{coil}}(i-1) + \Delta\varphi_{\text{shift}}^{\text{corner,coil}}$ ;  $\varphi_i^{(2)} = \varphi_i^{(1)} + \Delta\varphi_{\text{width}}^{\text{coil}}$ ;  
 $\Delta\varphi_{\text{shift}}^{\text{corner,coil}} = \Delta\varphi_{\text{shift}}^{\text{center,coil}} - 0.5\Delta\varphi_{\text{width}}^{\text{coil}}$  and the toroidal width and shifts for the corresponding coils are:  
 $\Delta\varphi_{\text{width}}^{\text{coil}} = 29.4^\circ$  (upper),  $20.9^\circ$  (middle),  $30.5^\circ$  (low);  
 $\Delta\varphi_{\text{shift}}^{\text{center,coil}} = 30^\circ$  (upper),  $26.7^\circ$  (middle),  $30^\circ$  (low),  
 $i = 1:9$ . The currents in the coils are calculated as:  
 $I_i = I_C \cos[-N(\varphi_i^{\text{coil}} - \Delta\Phi^{\text{coil}}) \cdot \pi/180]$ , where  $I_C$  is the peak current,  $\varphi_i^{\text{coil}} = \Delta\varphi_{\text{shift}}^{\text{center,coil}} + 40 \cdot (i-1)$ ,  $N$ —is the main toroidal number of the RMP spectrum needed and the phasing between coils  $\Delta\Phi^{\text{coil}}$  is taken from the linear MHD response by the code MARS-F optimization studies, which maximized the magnetic displacement near the X-point [21, 51]. Because of the different definition of the starting

toroidal angle in MARS-F and ERGOS codes for the phase shift between coils we used the formula:  $\Delta\Phi_{\text{ERGOS}}^{\text{coil,temp}} = \Delta\varphi_{\text{shift}}^{\text{center,coil}} - (\Delta\Phi_{\text{MARS}}^{\text{coil}} + 180^\circ)/N$ . The phase in the middle coil is taken to be zero both in MARS-F and ERGOS codes, so that the relative phasing can be calculated using formula:  $\Delta\Phi_{\text{ERGOS}}^{\text{mid,new}} = \Delta\Phi_{\text{ERGOS}}^{\text{mid,temp}} - k \cdot 360^\circ/N$ ;  $\Delta\Phi_{\text{ERGOS}}^{\text{coil}} = \Delta\Phi_{\text{ERGOS}}^{\text{coil,temp}} - \Delta\Phi_{\text{ERGOS}}^{\text{mid,new}}$ ;  $k = 1$ . The optimum phasing for each scenario (except for the 12.5 MA ‘non-optimum’ case which was done for comparison with linear and non-linear MHD codes, see section 6) are presented in table 1. Both codes ERGOS and MARS-F were successfully benchmarked for vacuum modelling to ensure that the same RMP coils geometry and vacuum fields (not presented here) were used.

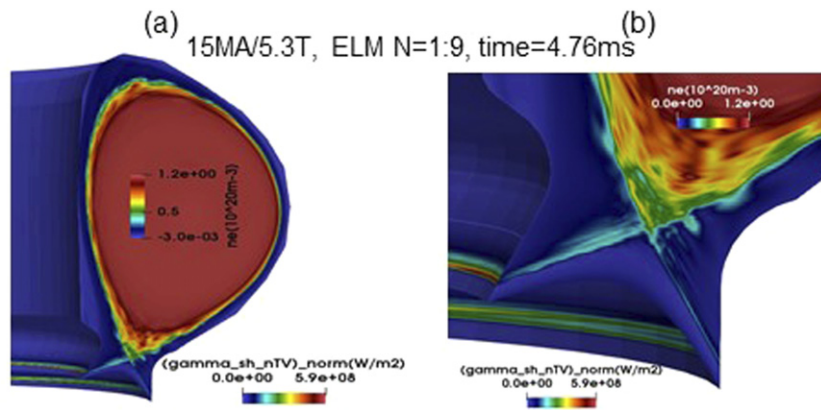


Figure 10. Density and maximum normal to the divertor plates heat flux at  $t = 4.76$  ms in natural ELM  $N = 1:9$  in 15 MA scenario.

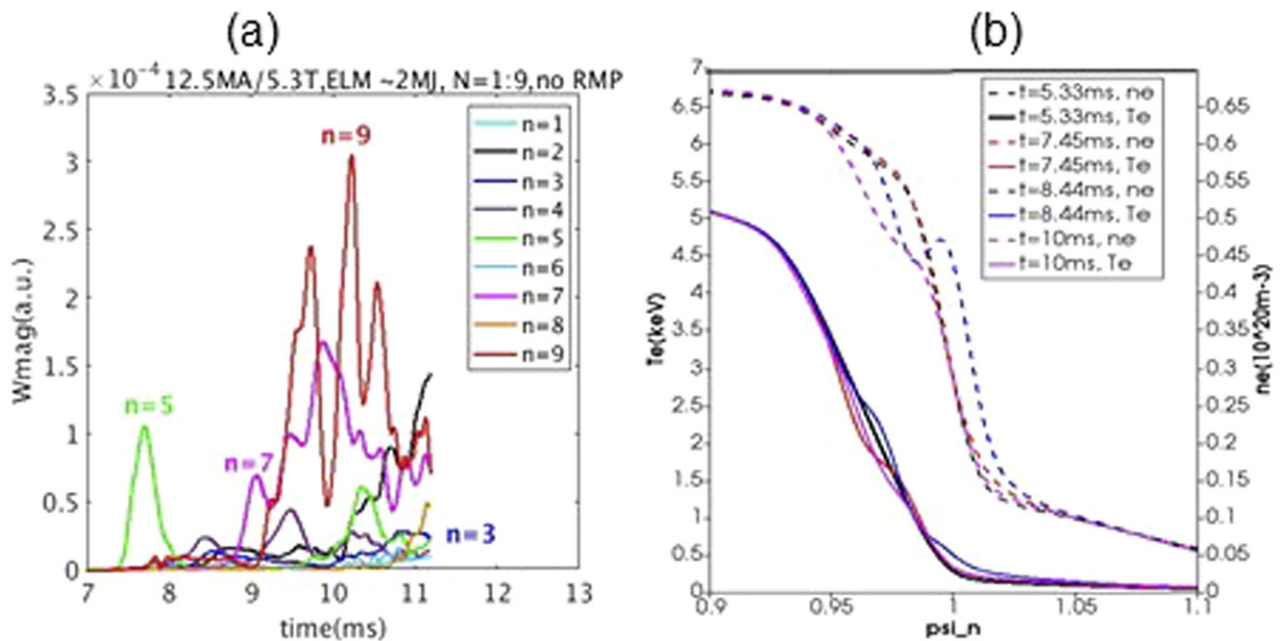
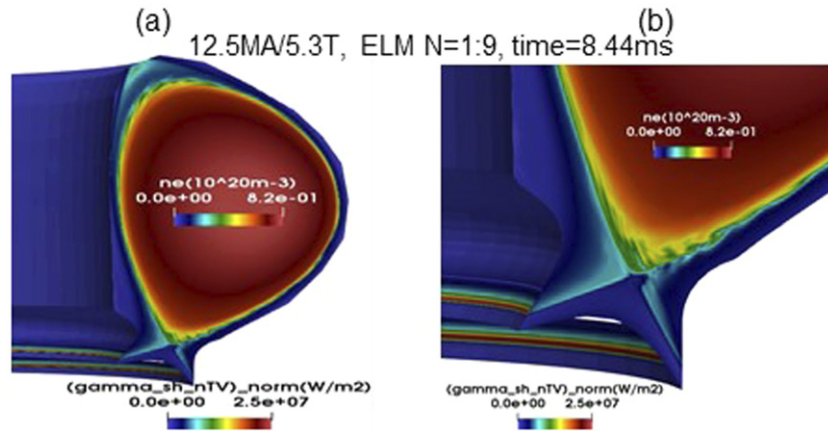


Figure 11. Magnetic energy in natural ELM with  $N = 1:9$  harmonics without RMPs in 12.5 MA scenario—(a) and changing electron temperature (in keV) and electron density (in  $10^{20} m^{-3}$ ) profiles during ELM crash—(b).

### 3. Modelling of natural ELMs without RMPs

For each ITER scenario considered, the stationary equilibrium with flows was obtained first on few ms time scale including only the  $N = 0$  harmonic as it was described before in section 2.2, then natural ELMs were modelled by adding  $N = 1, 2, 3, 4, 5, 6, 7, 8, 9$  harmonics initially at the noise level. The ELM size depends on the plasma parameters and in particular the pressure gradient, bootstrap current in the pedestal, which drives instability, but also on resistivity, viscosity and pedestal and SOL thermal conductivity which have numerical limits here. As a consequence only typical dynamics of ELMs and not the actual ELM size can be modelled. Note however that the ELM energy losses into the divertor modelled by JOREK code follow the Eich scaling [52], which was demonstrated in the modelling of the large number of JET ELMs where the ELM size corresponded to

the experimental values [53]. The magnetic energy perturbation of natural ELMs for 15 MA (Vtor(2)), and plasma profiles evolution during ELM crash are presented in figure 8. Note that in the 15 MA scenarios the low  $N$  harmonics ( $N = 2, 3, 4$ ) are the most unstable (figure 8(a)) which partly can justify the limited number of higher harmonics used here ( $N < 10$ ). The two fluid diamagnetic effects and toroidal rotations included in the model were found to be the most important factors in explaining the experimentally observed rotation of the peeling–ballooning modes before the ELM crash and in the inter-ELM phase [49]. In the non-linear phase of the ELM crash however this pre-ELM almost rigid rotation can be modified due to the non-linearly generated poloidal mean flow via Maxwell stress which sheared off the density filaments creating blobs which propagate in the SOL. This mechanism is described in details in [42, 49]. The rotation of modes before the ELM crash at time  $4 ms < t < 4.09 ms$  for 15 MA scenario



**Figure 12.** Density and maximum normal to the divertor plates heat flux at  $t = 8.44$  ms in natural ELM  $N = 1:9$  in 12.5 MA scenario.

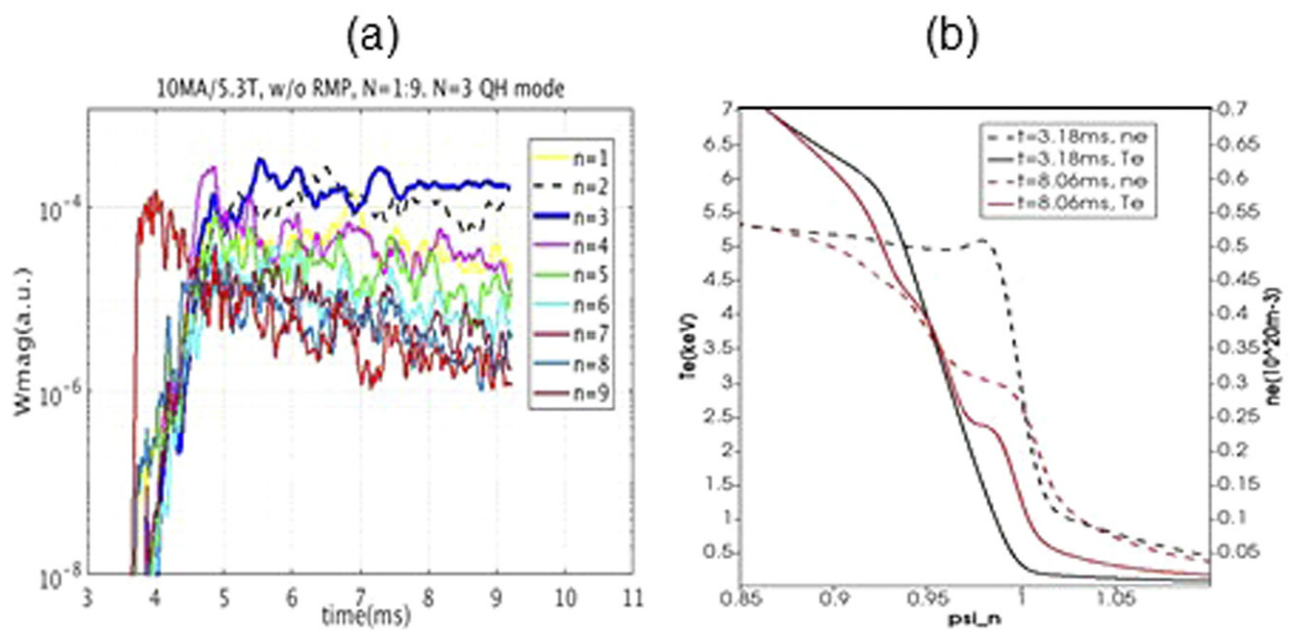


**Figure 13.** Magnetic energy—(a) and plasma profiles (b) in natural ELM  $N = 1:9$  in 10 MA scenario.

is presented in figure 9. As it will be shown later in section 4 while ELMs are suppressed by static RMPs this rotation stops which was also observed experimentally and modelled in [26] in AUG. The density convection and maximum divertor heat flux after the ELM crash at time  $t = 4.76$  ms for 15 MA scenario are presented in figure 10. Note that during the ELM more energy is deposited in inner divertor compared to outer which is typical picture observed in experiments [54, 55]. Even though the filaments due to the ballooning modes are mostly expelled from the outer region, the particle convection towards the inner region is enhanced by the diamagnetic flows as it was explained in JOREK modelling of ELMs with diamagnetic drifts [56].

In the 12.5 MA scenario the harmonic  $N = 5$  is most unstable first followed by triggering of the unstable modes  $N = 7, 9$  (figure 11(a)). In this scenario the ELM modelled with the same parameters was smaller and mostly convective with larger density losses compared to the temperature as it can

be seen in figure 11(b). Density filament and divertor heat flux in ELM crash in 12.5 MA scenario at  $t = 8.44$  ms are presented in figure 12.

In the high beta 10 MA scenario after the first crash due to  $N = 9$  harmonic the most unstable harmonic at the edge was  $N = 3$  producing QH-mode like behaviour without ELM crashes (figures 13(a) and (c)). The electron density and temperature profiles evolution is presented in figure 13(b). The rotation of the modes in 10 MA scenario is presented in figure 14(a), the density filaments and divertor heat flux at the time  $t = 8.06$  ms are shown in figure 14(b). The corresponding evolution of the thermal energy during the time of ELMs modelling for each scenario is presented in figure 15. In the 15 MA, 12.5 MA and 10 MA scenarios during the time of ELM modelling the energy losses were  $\sim 4$  MJ, 2 MJ and  $\sim 6$  MJ respectively. Note that the thermal energy is still evolving in all cases and these losses are not the total ELM size, because

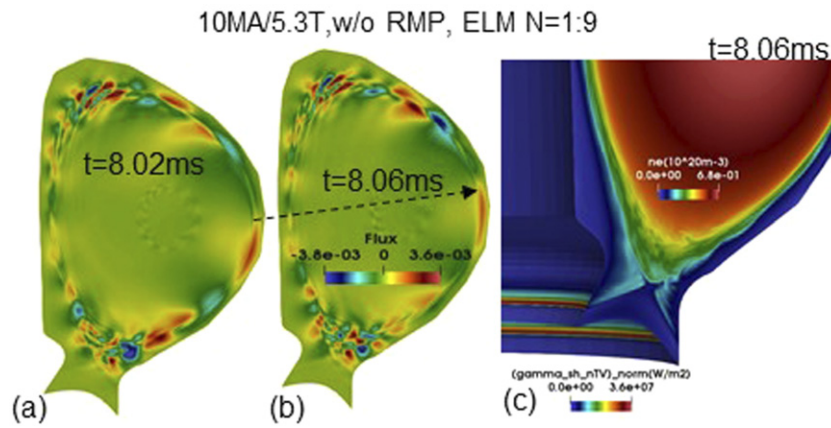


**Figure 14.** Modes  $N = 1:9$  rotation in natural ELM (main harmonic  $N = 3$ )—(a) and (b); electron density and normal to the divertor plates heat flux at  $t = 8.06$  ms in 10 MA scenario.

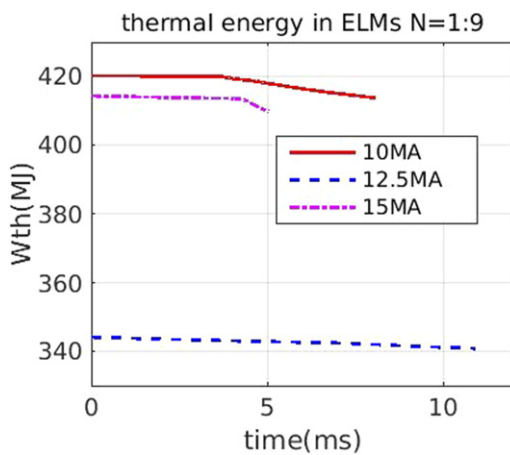


**Figure 15.** Thermal energy loss during time of modelling of the natural ELMs with harmonics  $N = 1:9$  in ITER scenarios 10 MA, 12.5 MA and 15 MA/5.3 T.

the main goal was to show that ELMs are unstable and can be stabilized by RMPs in all scenarios considered in this work.

#### 4. Modelling of ELMs with RMPs $N = 2, 3, 4$ in 15 MA/5.3 T scenario

The RMP current threshold studies were done for the 15 MA/5.3 T scenario. The magnetic energies of the modes  $N = 1:9$  during application of  $N = 3$  RMPs with different maximum RMP coils currents (from 0 kAt to 60 kAt) are shown in figure 16. Here the initial time without RMP was the same, but the harmonics energies are plotted here artificially shifted in time just for a better visual representation. One can see that for an RMP coil current larger than 45 kAt, the magnetic energy of RMPs ( $N = 3$  harmonic) and the non-linearly most strongly coupled harmonics ( $N = 6, 9$ ) are dominant. The other harmonics remain at a low noise level.

This corresponds to an ELM suppression picture similar to one found in [26, 31]. For lower RMP currents ( $< 45$  kAt) the growth rates of modes not strongly coupled to  $N = 3$  (e.g. 1, 2, 4, 5, 7, 8) are usually decreased by RMPs, however the ELMs

harmonics remain unstable, growing continuously and eventually produce an ELM crash. In the 15 MA/5.3 T scenario with increased toroidal rotation (figure 2(c)) very similar results of ELM suppression at lower toroidal rotation were obtained (figures 17(a) and (b)). In figure 17(a) only the initial stage of an ELM without RMP is shown. Note that with increased rotation (case  $V_{tor}(1)$ ) the most unstable modes were  $N = 6, 7, 8$  compared to the lower rotation  $V_{tor}(2)$  case (figure 8). For the case with RMPs at higher rotation we imposed vacuum harmonics  $N = 3, 6$  in the RMP spectrum at 60 kAt at the edge (note that  $N = 6$  energy is much lower) and  $N = 1:9$  modes were initialized when RMPs were established (figure 17(a)). This is a slightly different setup compared to figure 17(b), however the result is the same, ELMs are suppressed.

The results of application of RMPs separately with  $N = 2$ , and  $N = 4$  at maximum RMP current 60 kAt in the 15 MA scenario are presented in figure 18. Note that ELMs are strongly mitigated and crashes are avoided in all cases. The side harmonics  $N \times k$ , where  $N$  is the main RMP harmonic number and  $k$  is integer are more strongly coupled to RMPs and evolve similar to the main  $N$  of RMPs but at lower level (figures 17 and 18). Other side harmonics also are triggered via non-linear coupling and saturate, providing edge MHD turbulence instead of ELM crashes. Note that the saturation level is higher for  $N = 2$  and  $N = 4$  RMPs compared to the  $N = 3$  case (figures 17 and 18). The corresponding Poincare plots of plasma edge magnetic topology for  $N = 2, 3, 4$  at the last time of the modelling are presented in figure 19. As expected, the magnetic energy (and edge ergodization) of the main RMP harmonic at fixed current (here 60 kAt) decreases with toroidal number  $N$ , since harmonics with higher poloidal numbers ( $M$ ) are resonant at the edge ( $q_{res} = M/N$ ) and the RMP perturbation decreases with a distance from the RMP coils approximately as  $\sim 1/r^M$ . Note the characteristic lobes near the X-point and the narrow edge ergodic region typical for RMPs application pulses [11]. The electron densities

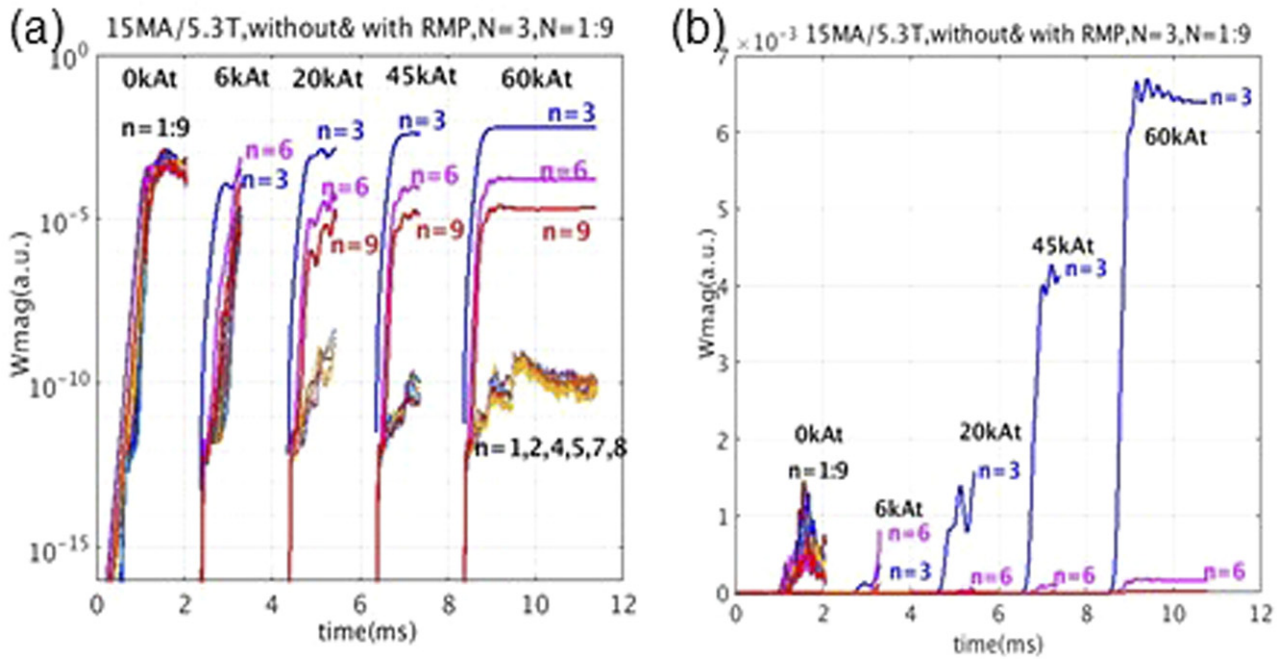


**Figure 16.** RMP current threshold studies in 15 MA scenario. Magnetic energies of  $N = 1:9$  modes with RMP  $N = 3$  at different maximum currents in RMP coils (0:60 kAt): (a)—in log scale; (b)—in linear scale. Each run starts by adding  $N = 1:9$  harmonics with RMP  $N = 3$  from the time of the equilibrium with flows (2.36 ms), but presented here shifted in time for better comparison.

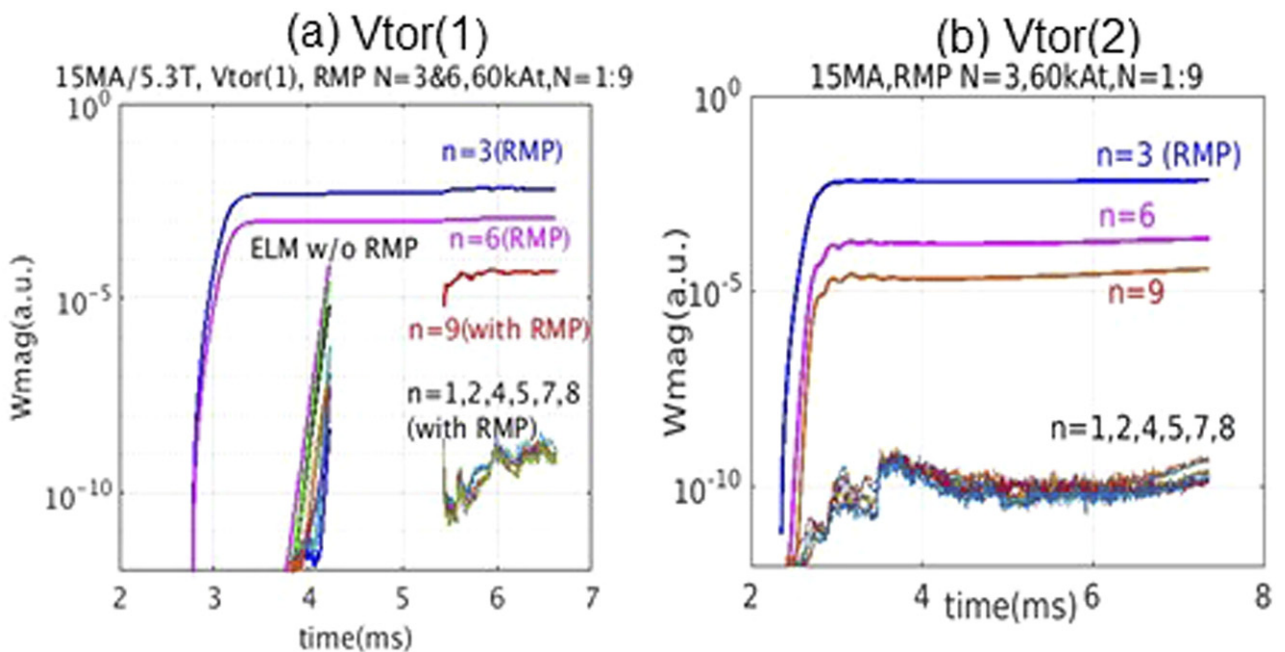


**Figure 17.** Comparison of magnetic energies of  $N = 1:9$  harmonics with RMP  $N = 3$ , 60 kAt in 15 MA scenario with different toroidal rotation profiles presented in figure 2: (a)—with stronger toroidal rotation  $V_{tor}(1)$ , (b)—and with slower rotation  $V_{tor}(2)$ . ELMs suppression is reached in both cases.

in ELM suppressed phase with RMPs  $N = 2, 3, 4$  at maximum RMP current 60 kAt are presented in figure 20 corresponding to times of the figure 19. A zoom of the electron density and temperature near X-point are presented in figure 21. Note that density convection and conductive energy transport mechanisms with RMPs are similar to natural ELMs [26, 31].

The plasma profiles at the mid-plane with and without RMPs for the time of modelling until the saturation of the magnetic energy of the modes are compared in figure 22. The energy transport slightly decreases with increasing  $N$  of RMPs, but density transport is almost the same for the all  $N-s$  modelled here. Note that here  $N = 1:9$  modes with different RMPs ( $N = 2, 3, 4$ ) were run for a few ms time after

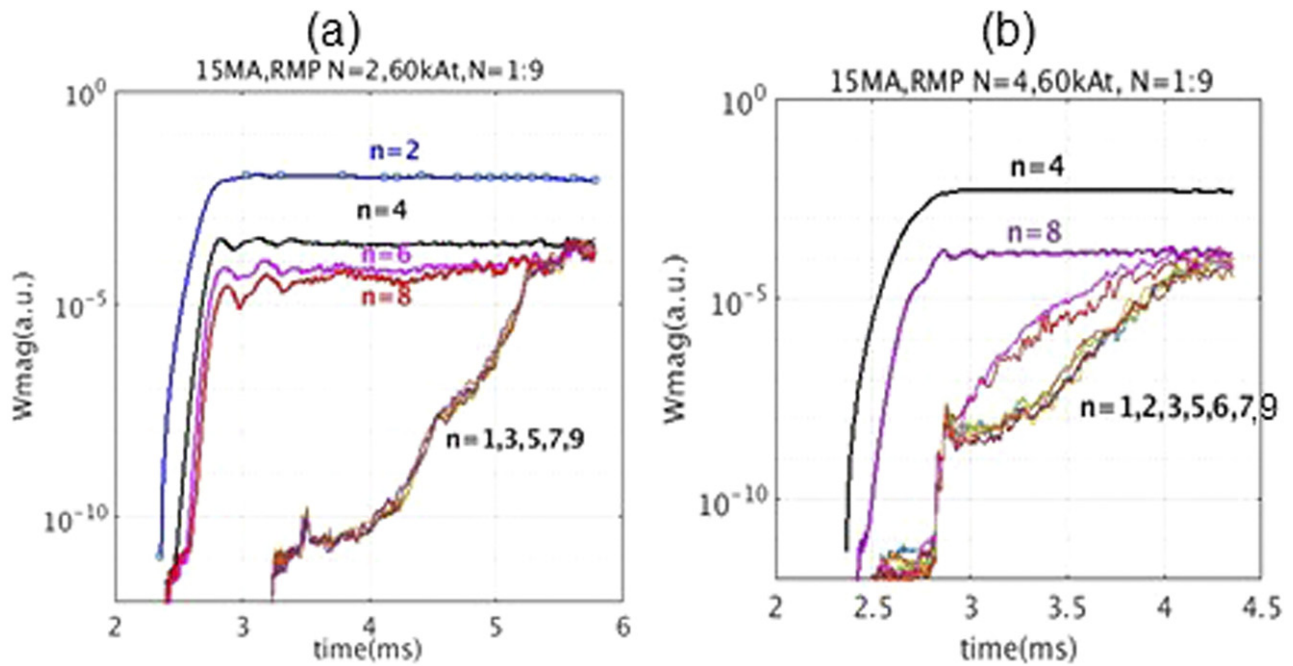


**Figure 18.** Magnetic energies of  $N = 1:9$  harmonics with RMP  $N = 2$ , 60 kAt (a) and  $N = 4$ , 60 kAt (b) in 15 MA scenario. Note that main harmonic with maximum energy corresponds to the  $N$  of RMPs followed in amplitude by mostly strongly coupled to RMPs  $N \times k$  harmonics and other harmonics saturate at relatively low level. The modelling here was done until the time of saturation of the modes corresponding to ELMs suppression.

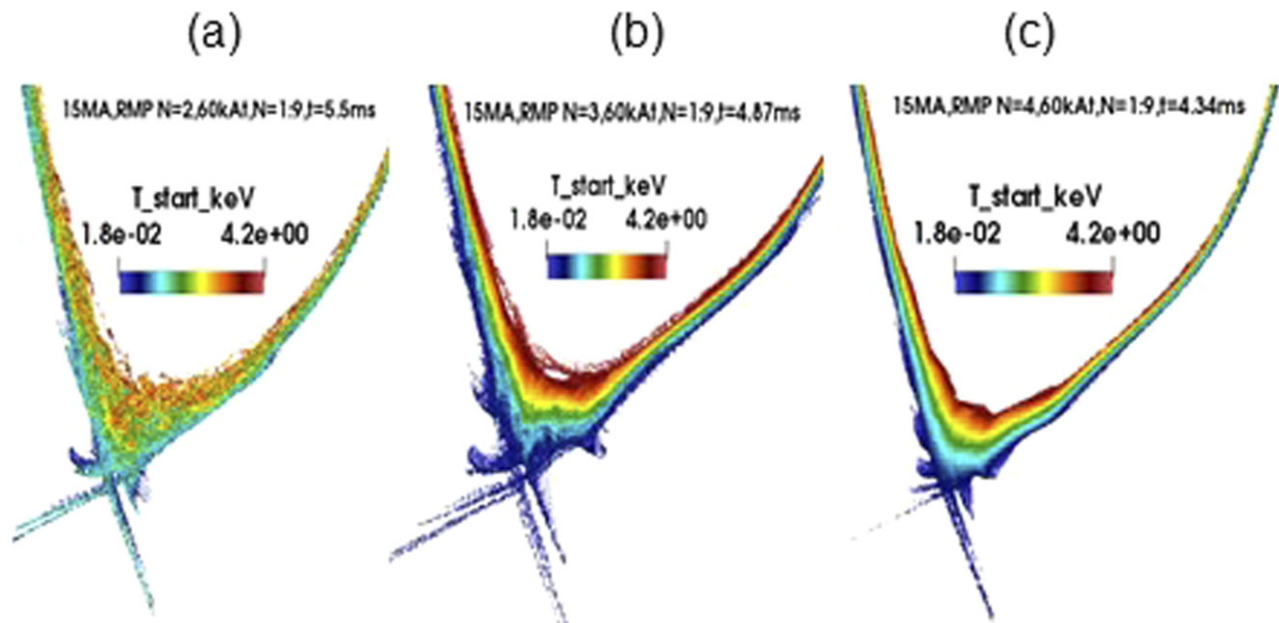


**Figure 19.** Edge magnetic topology at zero toroidal angle in 15 MA scenario with RMPs at maximum coils current 60 kAt and  $N = 2$  (a),  $N = 3$  (b) and  $N = 4$  (c) respectively. The colour bars indicates the electron temperature in the starting point of the field line in the core.

switching of RMPs until saturation of the magnetic energy, hence the presented here profiles are not final and stationary. The transient heat fluxes are large after switching on the RMPs, because plasma profiles and thermal energy are still evolving (figure 22(b)) and moreover no additional divertor physics, other than the sheath boundary conditions, is taken into account. The fully stationary profiles with RMPs were

not obtained here because of the small time step needed for modelling (few Alfvén times). The comparison of the divertor heat fluxes before the application of RMPs ( $t = 2.36$  ms) and with RMPs  $N = 3$ , 60 kAt at  $t = 6.19$  ms for 15 MA scenario is presented in figure 21 showing that with RMPs maximum divertor flux is transiently increased from  $16 \text{ MW m}^{-2}$  to  $47 \text{ MW m}^{-2}$  after 3.8 ms time. It is an important point to



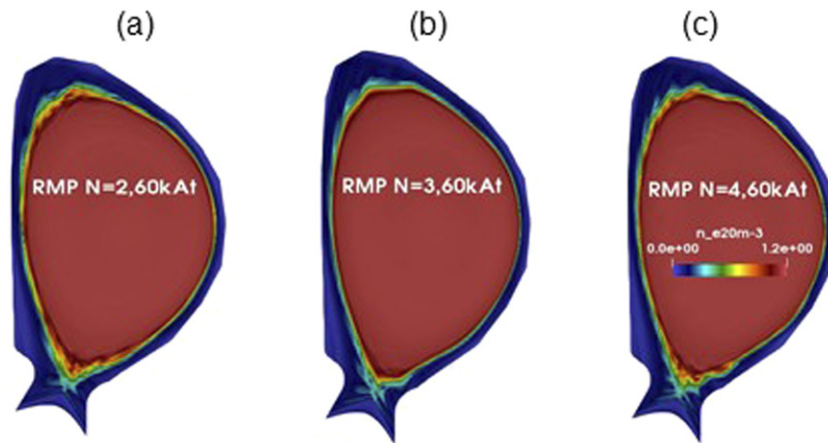


**Figure 20.** Electron density distribution in 15 MA scenario with RMPs at maximum coils current 60 kAt and RMP harmonic  $N = 2$  (a),  $N = 3$  (b) and  $N = 4$  (c) respectively. The common colour bar is presented in (c). In each case the time of modelling corresponds to maximum time in figures 17 and 18.

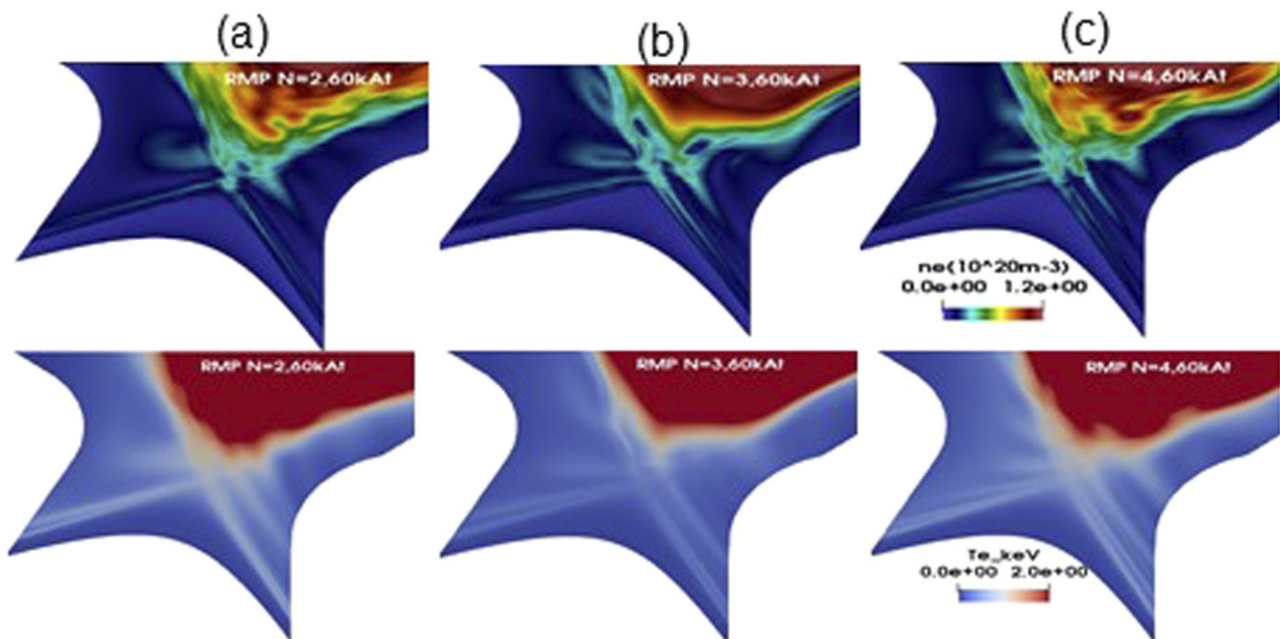


**Figure 21.** Electron density (upper row) and electron temperature (low row) distribution near X-point and divertor corresponding to cases presented in figure 20 for 15 MA scenario with RMPs at maximum coils current 60 kAt and RMP harmonic  $N = 2$  (a),  $N = 3$  (b) and  $N = 4$  (c) respectively. The common colour bars for density (upper) and temperature (low) are presented in (c).

stress here: RMPs release transiently heat and particles after switching on since the convective and conductive transport mechanisms in ergodic fields are very similar to natural ELMs. Heat flux splitting was observed both in inner and outer divertor (figure 23(b)). The detailed description of the divertor footprints and extrapolation to the stationary ELM suppressed conditions will be done in section 7. Note also that in the ELM suppressed phase the saturated modes are not rotating and are locked to the static RMPs as it is shown in figure 24 for  $N = 3$ , 60 kAt case.

### 5. Modelling of ELMs suppression by RMPs $N = 3$ , $N = 4$ in 10 MA/5.3 T and by RMPs $N = 3$ in 12.5 MA/5.3 T scenarios

The high beta 10 MA scenario is rather specific, since even without RMPs it exhibits features of a QH-mode without ELMs where  $N = 3$  remains unstable at plasma edge (figure 13), unlike the 12.5 MA scenario which resembles the 15 MA one. The application of RMPs at an RMP current amplitude of 20 kAt at  $N = 3$  (figure 25(a)) and  $N = 4$

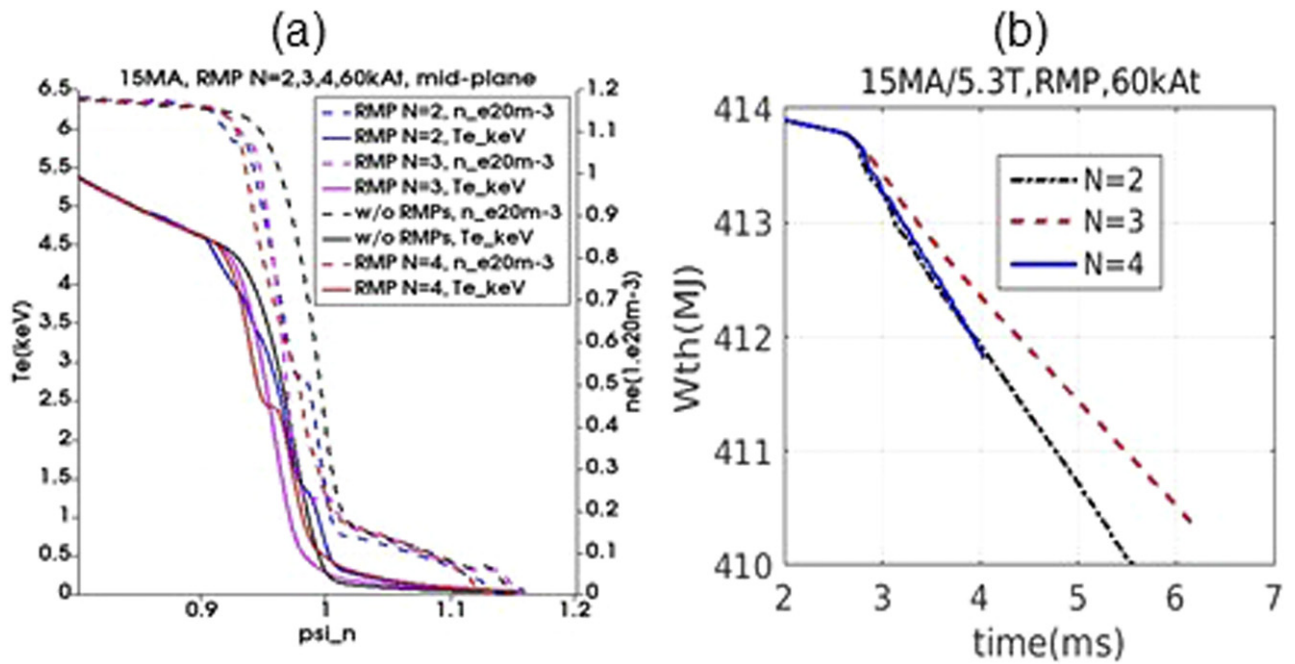


**Figure 22.** (a)—Plasma profiles for 15 MA scenario with RMPs  $N = 2, 3, 4$ , at maximum current 60 kAt,  $N = 1:9$ ; (b)—thermal energy evolution with RMPs  $N = 2, 3, 4$ , 60 kAt during time of modelling.

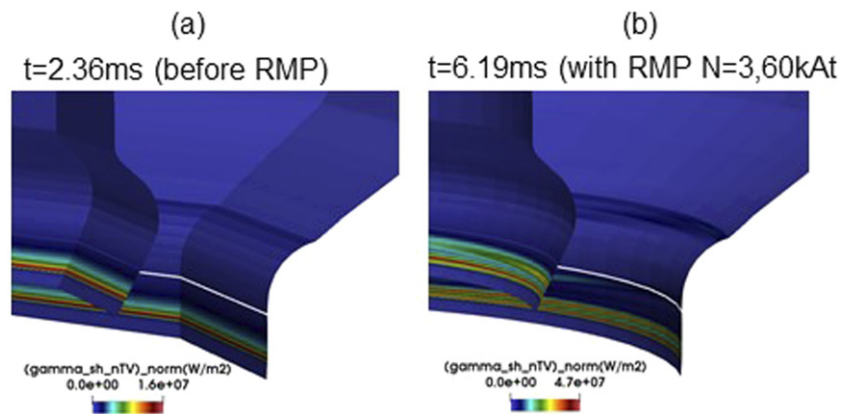


**Figure 23.** Non-normalized perpendicular to the divertor plates heat flux before RMPs (a) and with RMPs  $N = 3$ , 60 kAt in the maximum time of modelling ( $\sim 6.19$  ms) in 15 MA scenario. Note transient increase in the divertor heat flux after RMPs are switched on.

(figure 25(b)) also lead to QH-mode like behaviour in the 10 MA steady-state scenario, but with dominant  $N$  corresponding to applied RMPs. The magnetic topology corresponding to the maximum time of the modelling with  $N = 3$  and  $N = 4$  are presented in figures 26(a) and (b) respectively.

The density convection near  $X$ -point and plasma profiles with RMPs  $N = 3$  and  $N = 4$  in 10 MA/5.3 T scenario are presented in figure 27 showing strong density transport and almost no changes in temperature profile (figure 27(c), which is typical for QH-modes.

The magnetic energies of harmonics  $N = 1:9$  with RMP  $N = 3$  at 60 kAt in the 12.5 MA/5.3 T scenario are presented in figure 28, where ELM suppression is also obtained. The plasma profiles in the mid-plane without/with RMPs are presented in figure 29. Note the larger density transport

compared to energy transport, which is observed also in many RMP experiments.

## 6. Displacement near $X$ -point with linear (MARS-F) and non-linear (JOREK) plasma response modelling

In linear MHD studies with MARS-F code it was found that the external kink-peeling plasma response is an important factor for ELM suppression by RMPs [21]. At present, the maximum perpendicular magnetic surface displacement near  $X$ -point with linear MHD plasma response gives better predictions for ELM suppression in experiment [21] compared to the initial vacuum criterion of edge islands overlapping [5]. The non-linear modelling [26] also pointed out

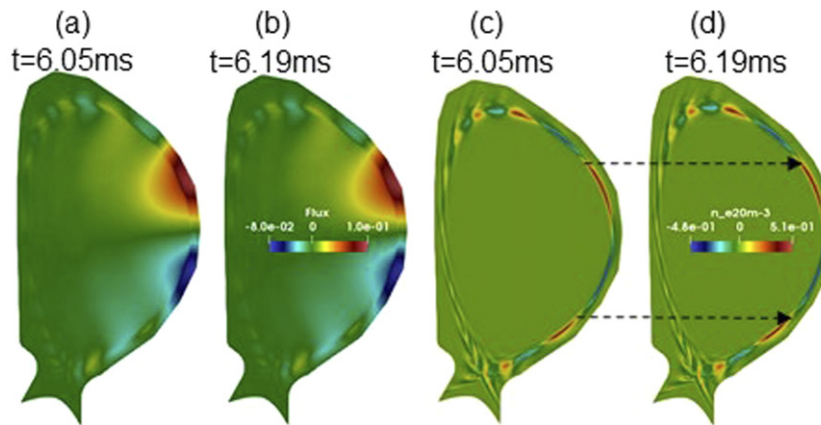


**Figure 24.** Modes  $N = 1:9$  locking with static RMPs  $N = 3$ , 60 kAt in 15 MA scenario in ELM suppressed phase.

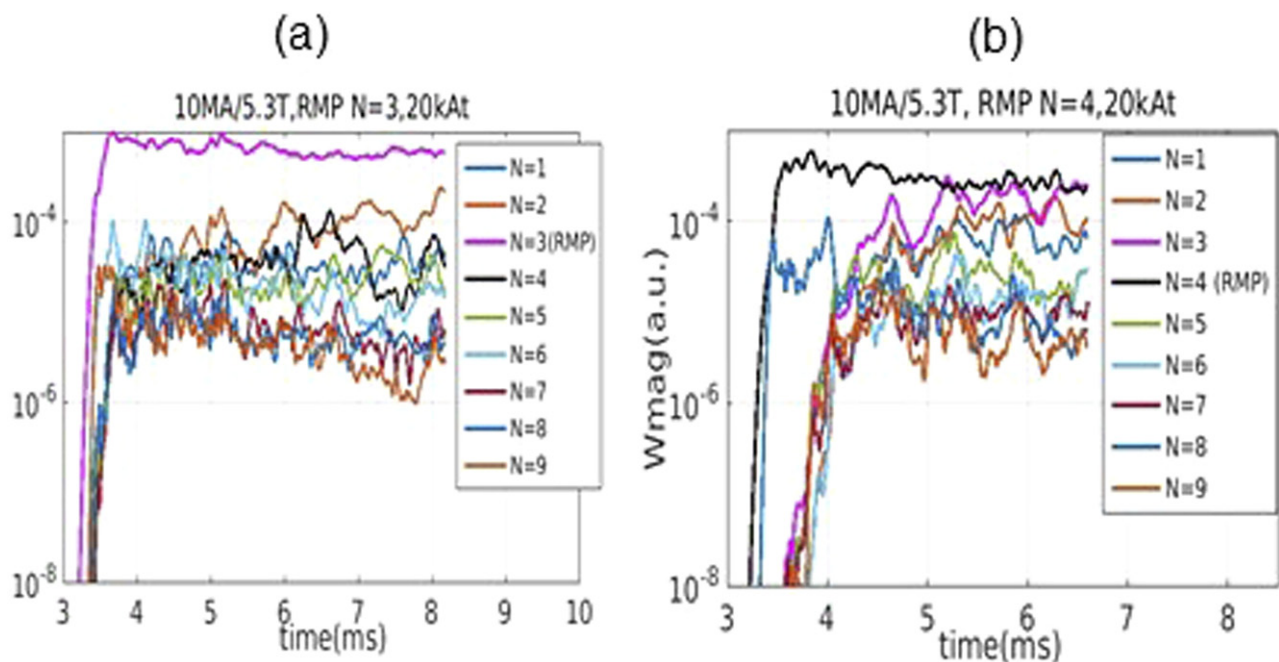


**Figure 25.** Magnetic energies of  $N = 1:9$  harmonics with RMP  $N = 3$ , 20 kAt (a) and  $N = 4$ , 20 kAt (b) in 10 MA scenario.

the role of the external kink plasma response in ELM suppression. Since the phasing of the RMP coils was optimised according to the MARS-F criterion [51], it is interesting to compare the computed displacements between the linear and non-linear MHD codes. Note, however, that properly speaking the magnetic displacement is difficult to define in non-linear MHD especially when the edge magnetic field is ergodic. Here we define the displacement in non-linear MHD as:  $\xi_{\perp} \approx \delta T_e / (\partial T_e / \partial \psi) / (\partial \psi / \partial r)$  also used in [57], where  $\delta T_e$  is electron temperature perturbation,  $\psi$ —is poloidal magnetic flux,  $r$ —is small radius. This approximation implies that electron temperature contours could represent the deformed magnetic surfaces, which will be checked below. The MARS-F code does not include separatrix in modelling which is truncated approximately at the normalized poloidal flux  $\psi_n \sim 0.99$ . In following comparison we consider that  $\psi_{n,\text{MARS-F}} = 1$  corresponds to  $\psi_{n,\text{JOREK}} = 0.99$ .

In the scenario 12.5 MA/5.3 T with optimum phasing (table 1) according to MARS-F, the displacement near the X-point at the last closed flux surface was about  $\sim 6$  mm at 60 kAt. The same value was obtained with the JOREK code, but at an early time of RMPs at  $\sim 6$  ms, i.e. in close to linear phase (figure 30). With the non-optimum phasing (table 1) the same displacement can be obtained by MARS-F simply by increasing the RMP current amplitude up to  $\sim 80$  kAt, since MARS-F is a linear code. These values were very similar in JOREK modelling at an early time ( $< 6.2$  ms) when the single RMP harmonic  $N = 3$  is established:  $\sim 6$  mm for optimum phasing at 60 kAt and  $\sim 8$  mm for the non-optimum phasing at 80 kAt (figure 30). However, for the later highly non-linear stage (here  $> 17$  ms) with multi-harmonics and self-consistently modified plasma profiles, the displacement in non-linear code JOREK as it is defined above is not valid anymore and is much larger in JOREK code

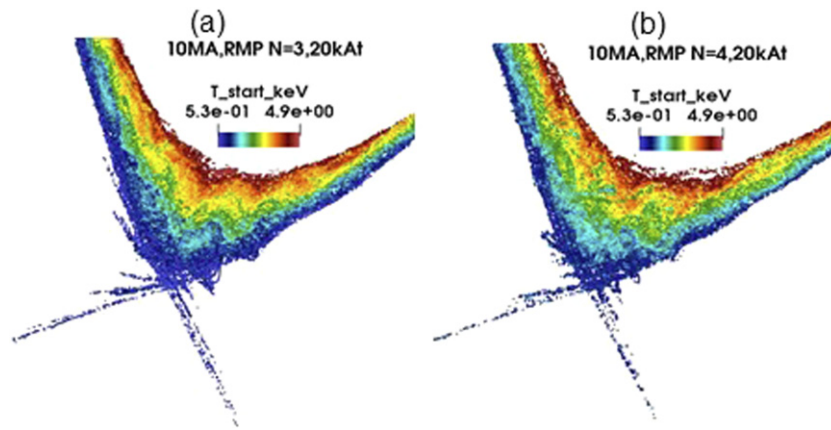


**Figure 26.** Magnetic topology at zero toroidal angle with RMPs  $N = 3$  (a) and  $N = 4$  (b) at 20 kAt RMP maximum current in 10 MA scenario. Colour bar indicate the electron temperature at the starting point of the field line inside the plasma.

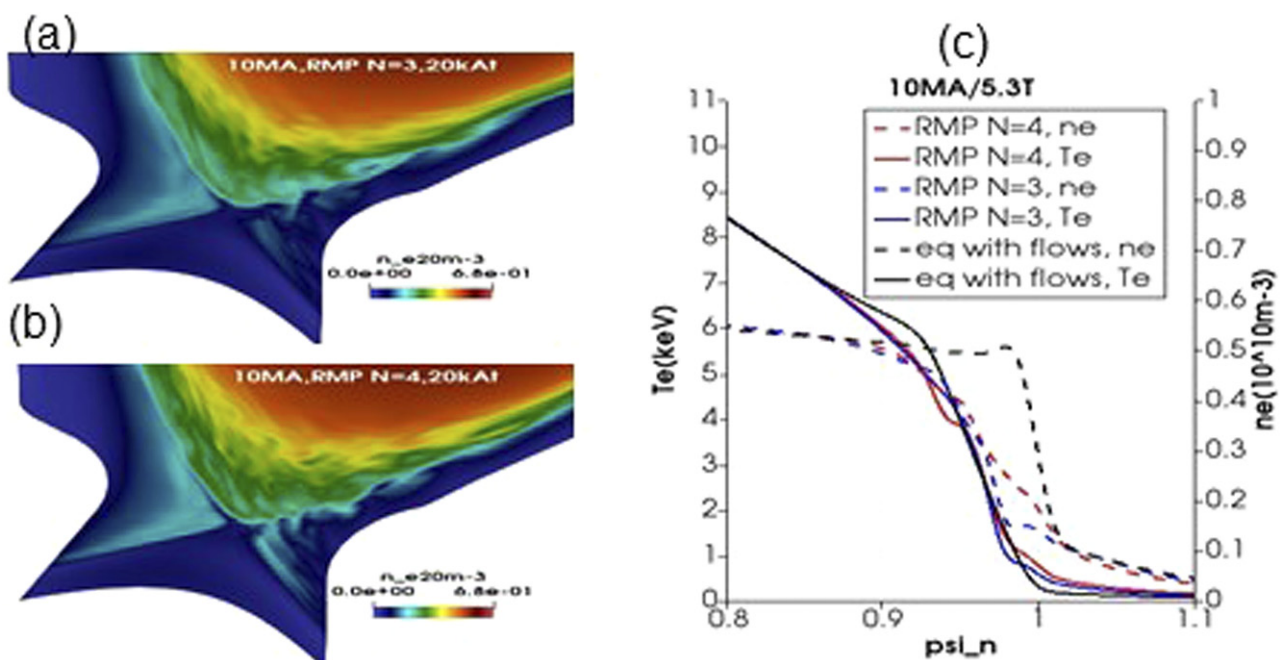


**Figure 27.** Density distribution near  $X$  point in 10 MA scenario with RMPs 20 kAt at  $N = 3$  (a),  $N = 4$  (b) and electron density and temperature profiles before and with RMPs respectively (c). Note larger density transport compared to the temperature with RMPs.

( $\sim 60$  mm, not shown here) than one in the linear MARS-F code.

## 7. Divertor footprints and power fluxes during ELM suppression

One important consequence of the application of RMPs is the resulting complex magnetic topology and splitting of the separatrix into a set of manifolds, seen in experiment as helical ‘lobes’ at the  $X$ -point [11, 38]. Crossing the divertor plates they form non-axisymmetric heat and particle fluxes which potentially can represent an issue for ITER, leading to local ‘hot spots’ and material erosion [38]. Rotation of the RMP field thus was considered as an option to spread out the heat and particle fluxes [2], but as a drawback it could lead to

significant mechanical stresses in RMP coils. Here we assess the heat and particle fluxes without rotation of the RMP fields. Note also that in the present model many essential divertor physics such as kinetic neutrals, recycling, radiation, etc, are missing. However the localization of divertor heat and particle fluxes with self consistently modelled RMPs with plasma response can be estimated here. The modelling time for all scenarios ( $\sim$ few tens of ms) is short compared to ITER confinement time ( $>3$  s), which is not presently accessible due to the computer time requirements for the small Alfvén-like time steps needed in the non-linear multi-harmonics MHD modelling with JOEUK code, even with a fully implicit scheme [42, 43]. The total heating power including fusion in the scenarios presented here was 171 MW at 10 MA, 153 MW at 12.5 MA and 128 MW at 15 MA/5.3 T. In the stationary

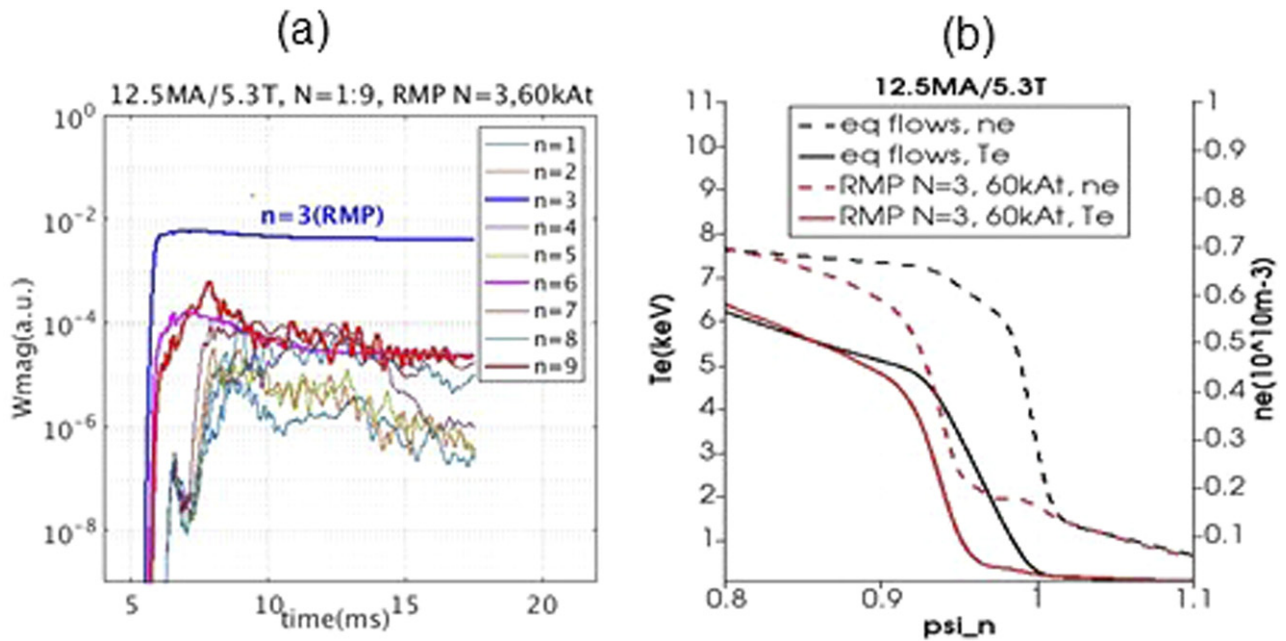


**Figure 28.** Magnetic energy of  $N = 1:9$  modes with RMP  $N = 3$ , 60 kAt in 12.5 MA scenario (a) and comparison of density and temperature profiles at the last time of modelling ( $\sim 17$  ms) with and without RMPs (b).

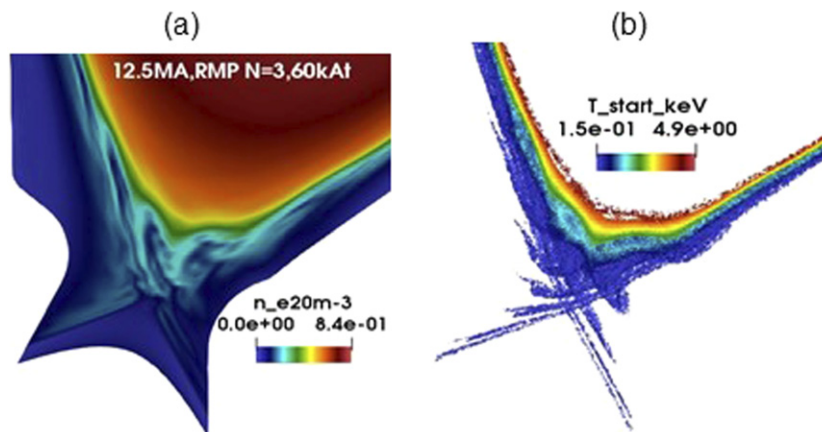


**Figure 29.** Density distribution (a) and magnetic topology (b) in 12.5 MA scenario.

phase with RMPs all power excluding losses goes to the divertor and walls. During the time of modelling with RMPs the plasma thermal energy is still evolving (figure 22), hence heat fluxes are transiently increased (figure 23). Since long confinement times were not accessible in MHD code, the stationary divertor heat fluxes have been extrapolated considering that magnetic footprints will be the same since magnetic energy of the modes reached the stationary phase. The extrapolation of heat fluxes to the stationary situation is done here using a normalization of the divertor heat fluxes to an assumed fixed power at  $P_{\text{div,st}} = 50$  MW power going to the divertor and walls based on the assumption that the divertor heat fluxes will be mitigated if divertor physics is taken into account and large part of power will be radiated in the core plasma and SOL [50]. The extrapolation to the stationary situation when the time derivative of thermal energy is zero:  $dW_{\text{th}}/dt = 0$

is done by multiplying the actual non-stationary perpendicular to the divertor target–baffle and first wall total heat flux ( $P_{\text{div,nst}} = \gamma_{\text{sh}}(T \cdot n_e \cdot \vec{V}_{\parallel}) \cdot \vec{n}$ ) by a factor  $P_{\text{div,st}}/P_{\text{div,nst}}$  (where  $\vec{n}$  is a normal to the surface vector, here  $T = T_e + T_i$ ). The heat fluxes normalized in this way versus toroidal angle along the divertor length for the 15 MA scenario without RMPs and with RMPs  $N = 2, 3, 4$  at 60 kAt are presented in figures 31 and 32. Here the uppermost point on these plots at the inner divertor baffle is taken as zero length along divertor  $L_{\text{div}} = 0$  and the lowest point of the outer divertor is at  $L_{\text{div}} = 0.411$  m. The non-normalized particle fluxes at the last time of modelling are presented in figures 33 and 34. Note that in this phase there are increased particle fluxes with RMPs which are not-stationary yet. One can see that the splitting of the footprints in the 15 MA/5.3 T scenario exhibits the  $N$ -symmetry of the main RMP harmonic (figures 31 and 32). A footprint maximum radial extension of  $\sim 20$  cm was observed in the inner

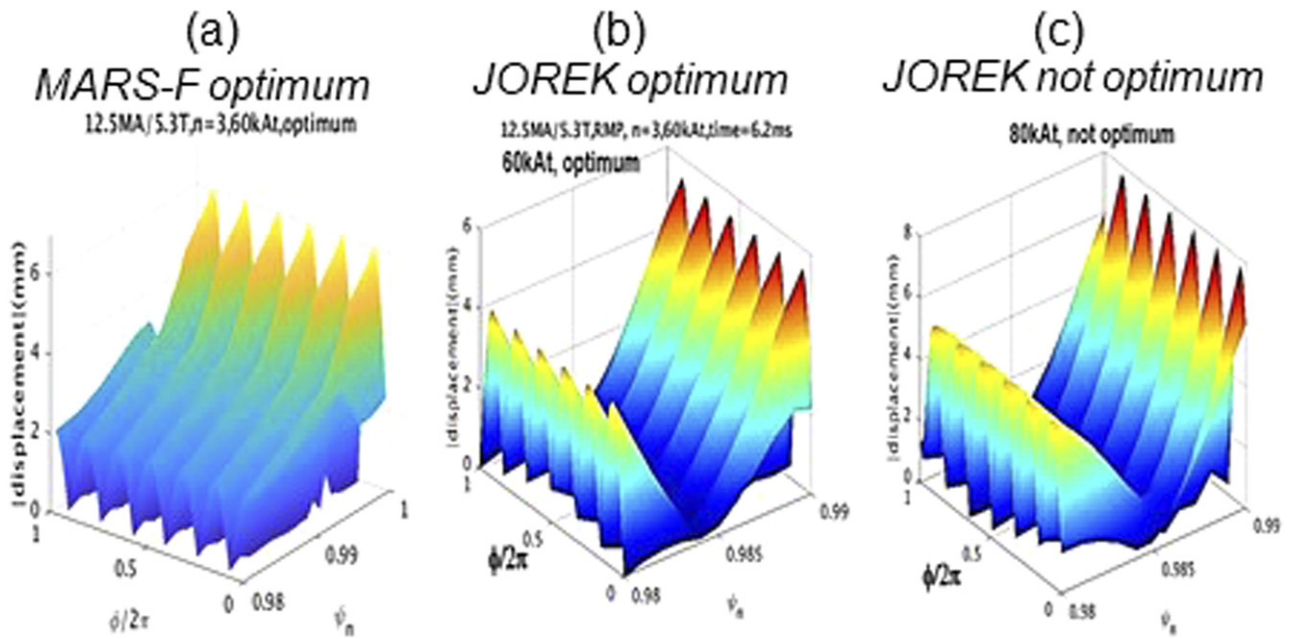


**Figure 30.** X-point displacement calculated by the linear MHD code MARS-F (a) and non-linear MHD code JOREK at time 6.2 ms (b) with optimum phasing (see table 1) of RMP  $N = 3$ , 60 kAt, in 12.5 MA scenario. Note that the computational boundary in MARS-F  $\psi_n = 1$  corresponds to  $\psi_n \sim 0.99$  in JOREK, since the separatrix is not taken into account in MARS-F code. The displacement near X-point calculated by JOREK with not-optimum phasing at 80 kAt is presented in (c).

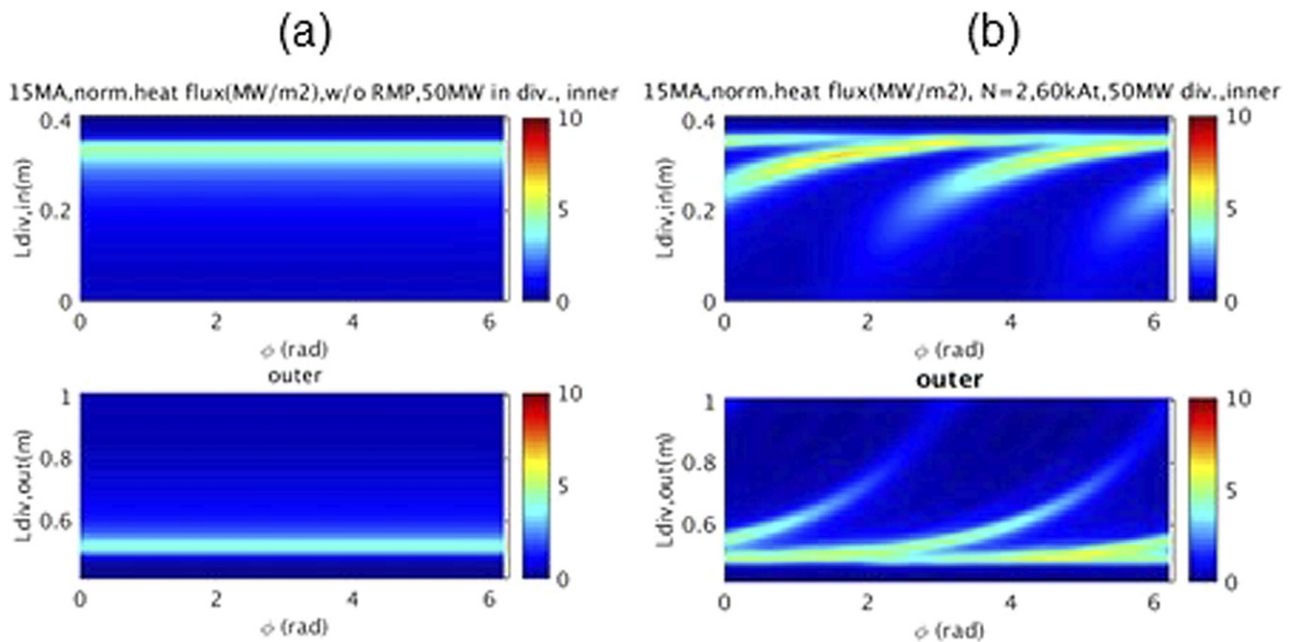


**Figure 31.** Stationary normalized divertor heat flux without RMPs and with RMPs  $N = 2$ , 60 kAt considering total power on the divertor/walls  $\sim 50$  MW in 15 MA scenario. Colour bars scales are the same from 0 to 10  $\text{MW m}^{-2}$  for better comparison of all cases.

divertor and of  $\sim 40$  cm in the outer divertor. At the outer divertor the heat fluxes with RMPs decrease from their maxima at the initial strike point value and the highest fluxes remain in the divertor target/baffle areas. Note, however, that at the outer divertor baffle/first wall boundary the heat flux can remain as high as  $\sim 1 \text{ MW m}^{-2}$  in stationary conditions (figures 31

and 32), which is within the power handling capability of ITER's first wall. This could be a potential concern for first wall loads at the start of ELM suppression, since the switch-on of the RMP coils leads to a partial loss of confinement (up to 20% in experiments [5–7]). Heat fluxes to PFCs will transiently increase before a new stationary situation with

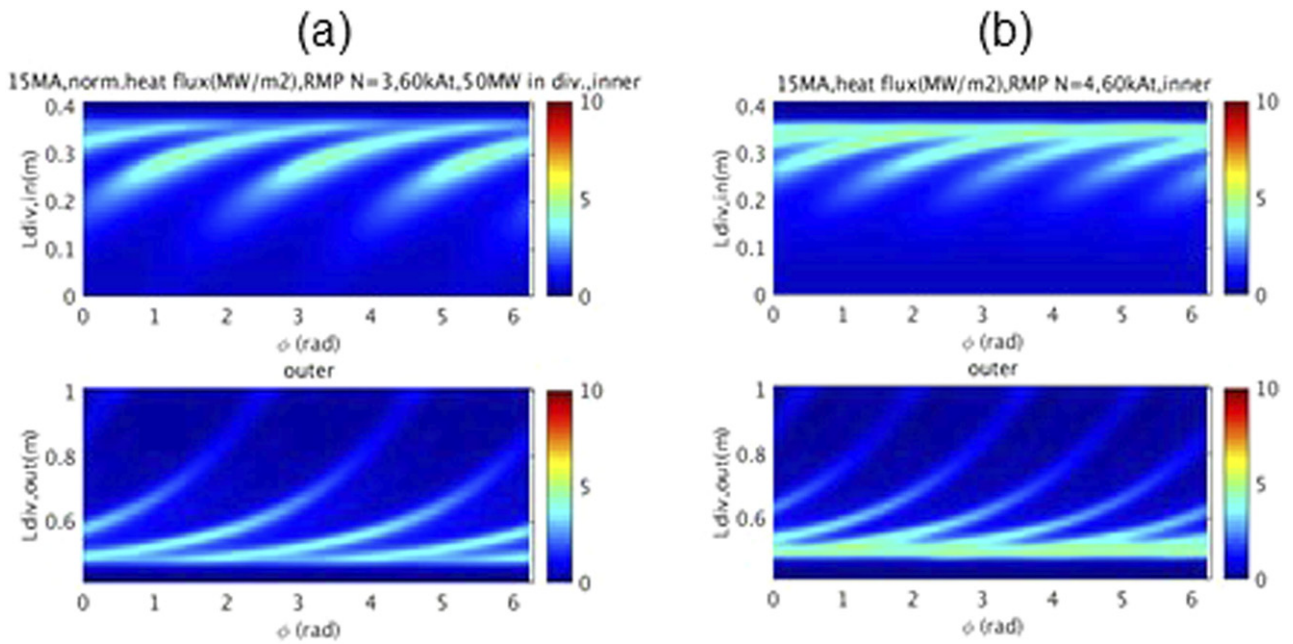


**Figure 32.** Stationary normalized divertor heat flux with RMPs  $N = 3$  (a) and  $N = 4$  (b) at 60 kAt considering total power on the divertor/walls  $\sim 50$  MW in 15 MA scenario. Colour bars scales are the same from 0 to 10  $\text{MW/m}^2$  for better comparison.

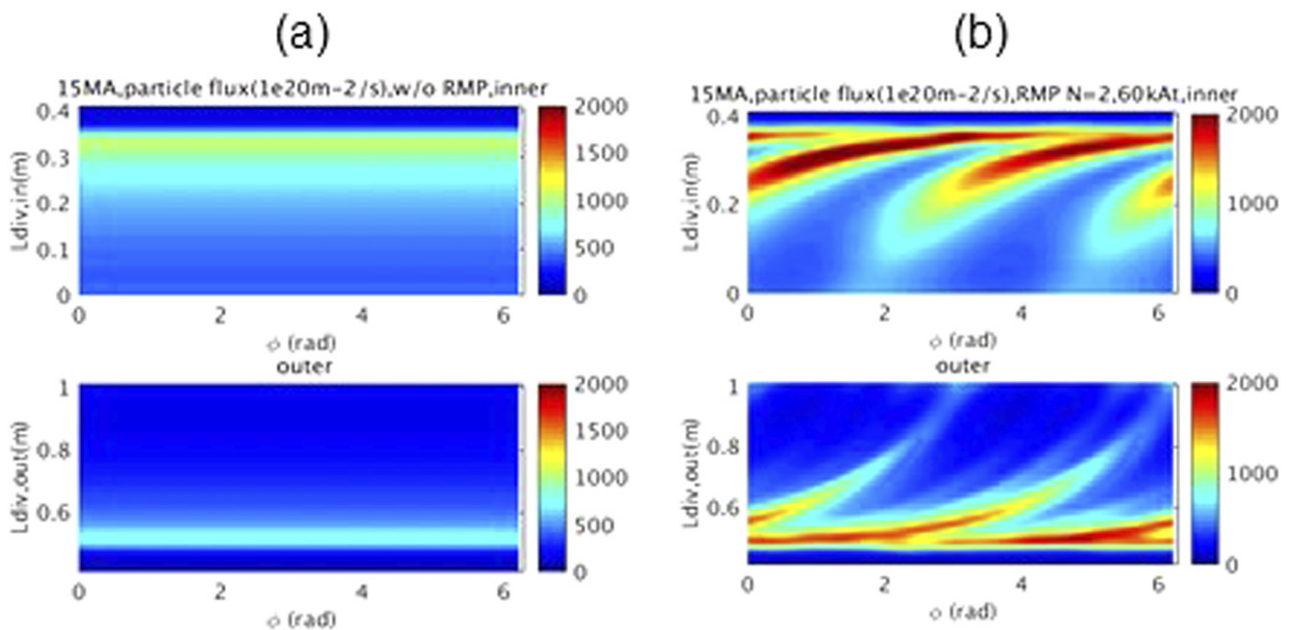


**Figure 33.** Particle fluxes without (a) and with RMPs  $N = 2$ , 60 kAt (b) in 15 MA scenario.

RMPs is reached as it is shown in figure 23 where non-stationary divertor heat fluxes after switching on of RMPs are presented. This fact should be considered to determine the more favorable time to switch-on the RMPs, i.e. before or soon after the L–H transition avoiding the first ELM, although optimization is required to avoid increasing the L–H power thresh-

old with RMPs. Modelling of such conditions is out of scope of the present paper. To mimic the effect of the slow rotation of RMPs to spread out the asymmetry in divertor footprints proposed in [2] during ELM suppression the toroidally averaged stationary divertor heat fluxes are presented in figure 35. However here we remind again that such rotation of RMP

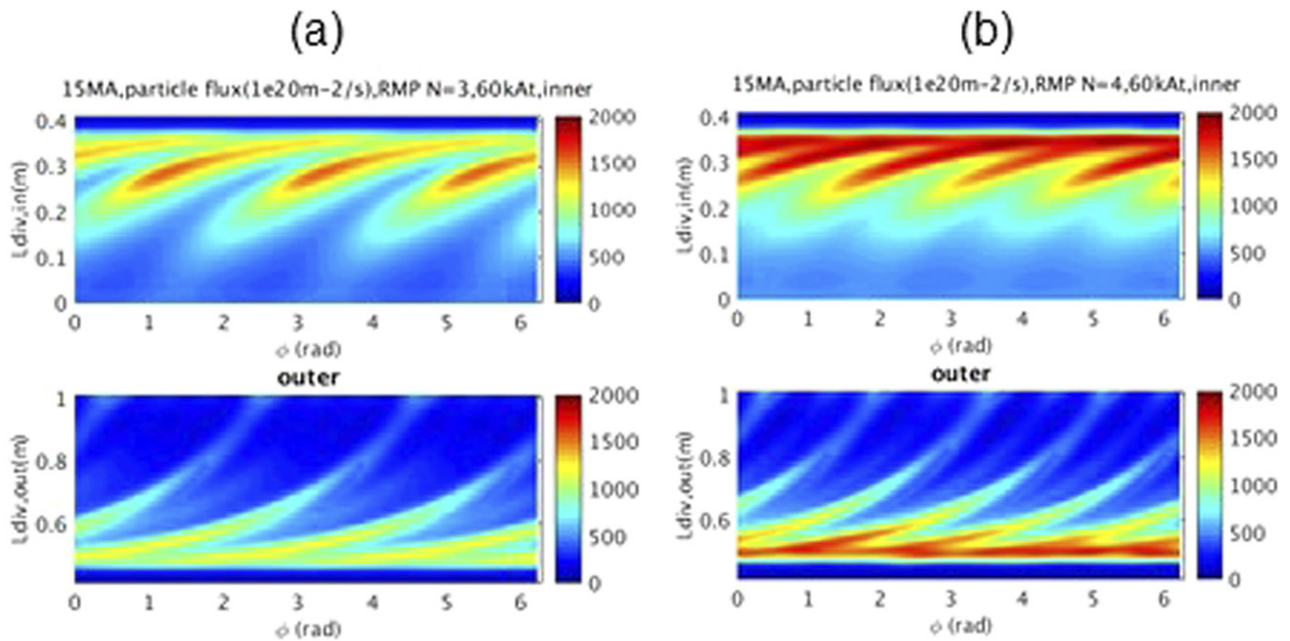


Figure 34. Particle fluxes with RMPs  $N = 3$  (a) and  $N = 4$  (b), at 60 kAt in 15 MA scenario.

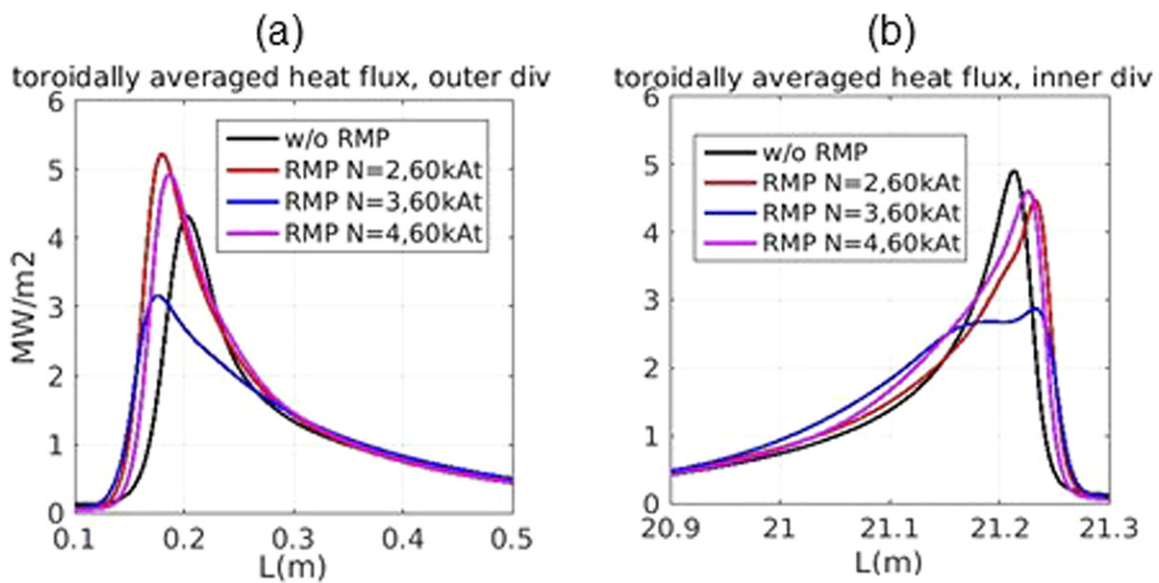
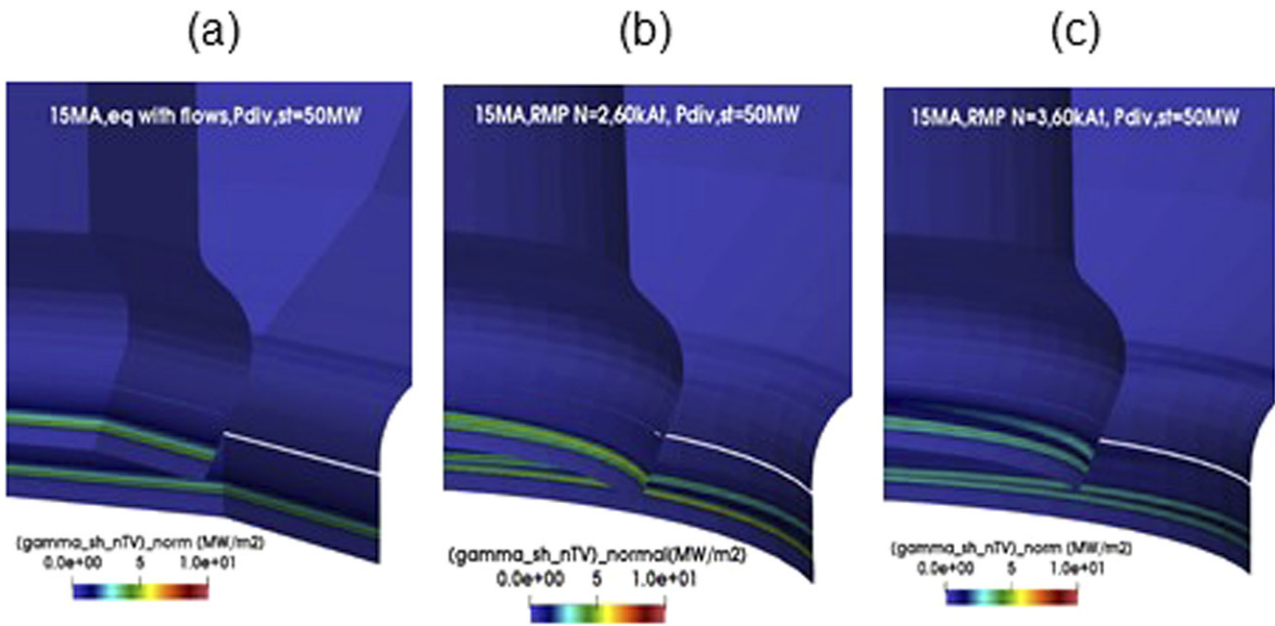


Figure 35. Toroidally averaged stationary normalized divertor heat fluxes in 15 MA scenario with RMPs  $N = 2, 3, 4$  at 60 kAt in outer divertor—(a) and inner divertor—(b) versus the length along the numerical boundary corresponding to the ITER divertor and wall starting from the lowest point of the grid in outer divertor which is considered  $L = 0$  here.

pattern could lead to large change of current amplitudes and hence large mechanical stress in RMP coils. The rigid rotation of RMPs with toroidal number  $N$  means change of phasing by  $\Delta\varphi_j = \pi/N$  in each coil during the rotation, leading to the maximum change of the current in the coil ( $i$ ) in time by  $I_{ij} = I_{\max,i} \cos(N(\varphi_i - \Delta\varphi_j))$  and hence change in the phase  $\pi$

and current change is at least twice the amplitude of the maximum current in the corresponding RMP coil. The stationary normalized ( $P_{\text{div,st}} = 50$  MW) heat fluxes in all scenarios in the divertor area are presented in figures 36 and 37, where it is shown that in the stationary conditions the 3D divertor heat fluxes remain within the material limits.





**Figure 36.** Normalized divertor heat fluxes without RMPs—(a), with RMPs  $N = 2$ —(b),  $N = 3$ —(c) at 60 kAt in 15 MA scenario. Colour bars scales are the same from 0 to 10  $\text{MW}/\text{m}^{-2}$  for better comparison.

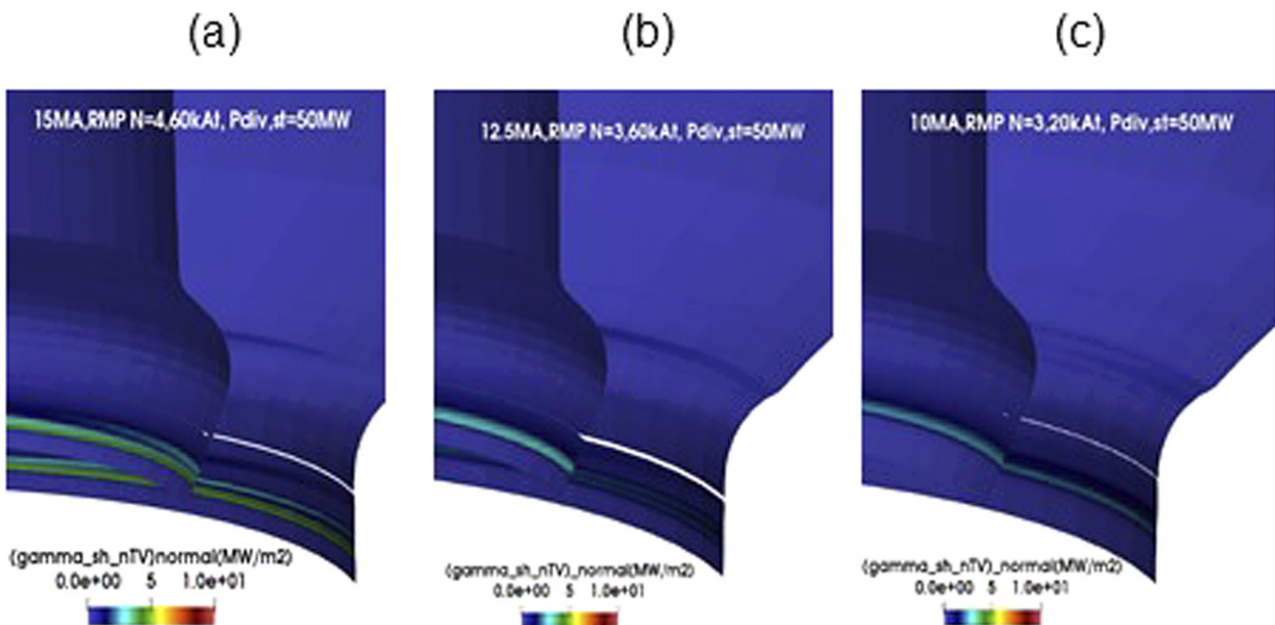


**Figure 37.** Normalized divertor heat fluxes with RMPs  $N = 4$ , 60 kAt in 15 MA/5.3 T scenario—(a), with RMPs  $N = 3$ , 60 kAt in 12.5 MA scenario—(b) and with RMPs  $N = 3$ , 20 kAt in 10 MA scenario—(c). Colour bars scales are the same from 0 to 10  $\text{MW}/\text{m}^{-2}$  for better comparison.

## 8. Conclusions

The interaction of ELMs with RMPs was studied in multi-harmonic non-linear MHD simulations for ITER scenarios 15 MA, 12.5 MA, 10 MA/5.3 T. The RMP spectrum, optimized by the linear resistive MHD MARS-F code, with the main toroidal harmonics  $N = 2$ ,  $N = 3$  and  $N = 4$  were used (table 1). In the 15 MA scenario, the threshold for ELM suppression was found to be at an RMP coil current of  $\sim 45$  kAt–60 kAt,

compared with a maximum coil capacity of 90 kAt. RMPs non-linearly generate continuous MHD turbulent transport stabilizing ELMs in all scenarios. In the high beta poloidal 10 MA/5.3 T steady-state scenario without RMPs an  $N = 3$  rotating QH-mode was observed. With  $N = 3$ ,  $N = 4$  RMPs at 20 kAt similar behaviour is observed with dominant low  $N$ -modes at the edge  $N = 3$  and  $N = 4$  respectively. The 3D divertor heat and particle fluxes demonstrate the typical splitting with the main toroidal symmetry of the RMP

spectrum. The maximum radial extension of the 3D heat fluxes in 15 MA/5.3 T scenario at maximum RMP coils current 60 kAt ( $N = 2, 3, 4$ ) was about  $\sim 20$  cm at the inner divertor and  $\sim 40$  cm at the outer divertor with the heat fluxes decreasing further out from the strike point from  $\sim 5$ – $6$  MW  $m^{-2}$  reaching  $\sim 1$  MW  $m^{-2}$  at the outer divertor baffle/first wall interface in the stationary RMP regime (assuming a total power to the divertor/first wall of  $\sim 50$  MW). Note that at the LFS heat fluxes with RMPs mainly remains within the divertor target/baffle area and within the design limits for divertor target ( $< 10$  MW  $m^{-2}$ ), baffle ( $< 5$  MW  $m^{-2}$ ) and first wall ( $\sim 1$  MW  $m^{-2}$ ) for all scenarios. However in transient regimes when RMPs are switched on, part of the plasma thermal energy is lost and these heat fluxes can be much larger; optimization of RMP switch-on needs to be studied further with respect to the ensuing power fluxes and L–H access.

## Acknowledgments

The present paper is dedicated to our long term co-author and dear colleague Todd Evans who worked on this paper, but sadly passed away during the writing. Todd Evans experimental and modelling work was outstanding and opened the way to ELMs control by RMPs in ITER. The authors would like to thank the whole JOEKE Team for collaborations and fruitful discussions. Part of this work has been carried out within the framework of the EUROfusion Consortium and has received funding from the Euratom research and training program 2014–2018 and 2019–2020 under Grant Agreement No. 633053 and the ITER IO Contract No. IO/19/CT/4300001845. The views and opinions expressed herein do not necessarily reflect those of the European Commission. ITER is the Nuclear Facility, INB No. 174. The views and opinions expressed herein do not necessarily reflect those of the ITER Organization. This publication is provided for scientific purposes only. Its content should not be considered as commitments from the ITER Organization as a nuclear operator in the frame of the licensing process. This work was carried out the Marconi-Fusion supercomputer operated by CINECA.

## ORCID iDs

Y.Q. Liu  <https://orcid.org/0000-0002-8192-8411>  
 T.E. Evans  <https://orcid.org/0000-0002-8357-5859>  
 A. Loarte  <https://orcid.org/0000-0001-9592-1117>  
 S.D. Pinches  <https://orcid.org/0000-0003-0132-945X>  
 S.K. Kim  <https://orcid.org/0000-0002-0701-8962>  
 S. Futatani  <https://orcid.org/0000-0001-5742-5454>

## References

- [1] Hawryluk R. et al 2009 *Nucl. Fusion* **49** 065012
- [2] Loarte A. et al 2014 *Nucl. Fusion* **54** 033007
- [3] Becoulet M. et al 2003 *Plasma Phys. Control. Fusion* **45** A93–113
- [4] Eich T. et al 2005 *J. Nucl. Mater.* **337–339** 669–76
- [5] Fenstermacher M.E. et al 2008 *Phys. Plasmas* **15** 056122
- [6] Evans T. et al 2004 *Phys. Rev. Lett.* **92** 235003
- [7] Liang Y. et al 2007 *Phys. Rev. Lett.* **98** 265004
- [8] Nazikian R. et al 2015 *Phys. Rev. Lett.* **114** 105002
- [9] Suttrop W. et al 2011 *Phys. Rev. Lett.* **106** 225004
- [10] Jeon Y.M. et al 2012 *Phys. Rev. Lett.* **109** 035004
- [11] Kirk A. et al 2012 *Phys. Rev. Lett.* **108** 255003
- [12] Sun Y. et al 2016 *Phys. Rev. Lett.* **117** 115001
- [13] Schaffer M.J., Menard J.E., Aldan M.P., Bialek J.M., Evans T.E. and Moyer R.A. 2008 *Nucl. Fusion* **48** 024004
- [14] Evans T.E. et al 2013 *Nucl. Fusion* **53** 093029
- [15] Becoulet M. et al 2008 *Nucl. Fusion* **48** 024003
- [16] Fitzpatrick R. 1998 *Phys. Plasmas* **5** 3325
- [17] Strauss H.R., Sugiyama L., Park G.Y., Chang C.S., Ku S. and Joseph I. 2009 *Nucl. Fusion* **49** 055025
- [18] Orain F. et al 2013 *Phys. Plasmas* **20** 102510
- [19] Becoulet M. et al 2014 *Phys. Rev. Lett.* **113** 115001
- [20] Ferraro N.M. 2012 *Phys. Plasmas* **19** 056105
- [21] Liu Y. et al 2016 *Plasma Phys. Control. Fusion* **58** 114005
- [22] Park J.-K. et al 2018 *Nat. Phys.* **14** 1223–8
- [23] Becoulet M. et al 2012 *Nucl. Fusion* **52** 054003
- [24] Garofalo A. et al 2008 *Phys. Rev. Lett.* **101** 195005
- [25] Nardon E. et al 2010 *Nucl. Fusion* **50** 034002
- [26] Orain F. et al 2019 *Phys. Plasmas* **26** 042503
- [27] Shaing K. 2003 *Phys. Plasmas* **10** 1443
- [28] Becoulet M. et al 2009 *Nucl. Fusion* **49** 085011
- [29] Hu Q.M. et al 2021 *Phys. Plasmas* **28** 052505
- [30] Hager R., Chang C.S., Ferraro N.M. and Nazikian R. 2020 *Phys. Plasmas* **27** 062301
- [31] Kim S.K. et al 2020 *Nucl. Fusion* **60** 02600
- [32] Harrison J.R., Kirk A., Chapman I.T., Cahyna P., Liu Y., Nardon E. and Thornton A.J. 2014 *Nucl. Fusion* **54** 064015
- [33] Jakubowski M.W. et al 2009 *Nucl. Fusion* **49** 095013
- [34] Ahn J.-W., Canik J.M., Soukhanovskii V.A., Maingi R. and Battaglia D.J. 2010 *Nucl. Fusion* **50** 045010
- [35] Thornton A.J., Kirk A., Cahyna P., Chapman I.T., Harrison J.R. and Liu Y. 2014 *Nucl. Fusion* **54** 064011
- [36] Suttrop W. et al 2018 *Nucl. Fusion* **58** 096031
- [37] Kukushkin A.S., Pacher H.D., Kotov V., Pacher G.W. and Reiter D. 2011 *Fusion Eng. Des.* **86** 2865–73
- [38] Frerichs H., Schmitz O., Bonnin X., Loarte A., Feng Y., Li L., Liu Y.Q. and Reiter D. 2020 *Phys. Rev. Lett.* **125** 155001
- [39] Wesson J. 2004 *Tokamaks* (Oxford: Clarendon)
- [40] Chatey A. 2020 *Nucl. Fusion* **60** 124007
- [41] Xu X.Q. et al 2010 *Phys. Rev. Lett.* **105** 175005
- [42] Huysmans G.T.A. and Grazny O. 2007 *Nucl. Fusion* **47** 659–66
- [43] Hoelzl M. et al 2021 *Nucl. Fusion* **61** 065001
- [44] Stangeby P. 2000 *The plasma boundary of magnetic fusion devices (Plasma Physics Series)* (Bristol: IOP Publishing) p 703
- [45] Spitzer L. and Härm R. 1953 *Phys. Rev.* **89** 977
- [46] Bale S.D., Pulupa M., Salem C., Chen C.H.K. and Quataert E. 2013 *Astrophys. J.* **769** L22
- [47] Becoulet M. et al 2005 *Nucl. Fusion* **45** 1284–92
- [48] Smith S.F. et al 2020 *Nucl. Fusion* **60** 066002
- [49] Becoulet M. et al 2017 *Nucl. Fusion* **57** 116059
- [50] Polevoi A.R., Shimada M., Sugihara M., Igitkhanov Y.L., Mukhovatov V.S., Kukushkin A.S., Medvedev S.Y., Zvonkov A.V. and Ivanov A.A. 2005 *Nucl. Fusion* **45** 1451
- [51] Liu Y. et al 2020 Towards prediction of ELM control by RMP in ITER based on linear and quasi linear plasma response 28th IAEA FEC 28th IAEA Fusion Energy Conf. (FEC 2020) (Virtual, 10–15 May 2021) (<http://conference.iaea.org/event/214/contributions/17556>)
- [52] Eich T., Sieglin B., Thornton A.J., Faitsch M., Kirk A., Herrmann A. and Suttrop W. 2017 *Nucl. Mater. Energy* **12** 84–90
- [53] Pamela S.J.P. et al 2017 *Nucl. Fusion* **57** 076006

- [54] Pitts R.A., Andrew P., Arnoux G., Eich T., Fundamenski W., Huber A., Silva C. and Tskhakaya D. 2007 *Nucl. Fusion* **47** 1437
- [55] Eich T., Herrmann A. and Neuhauser J. (ASDEX Upgrade Team) 2003 *Phys. Rev. Lett.* **91** 195003
- [56] Orain F. *et al* 2015 *Plasma Phys. Control. Fusion* **57** 014020
- [57] Park J.K. *et al* 62nd Annual Meeting of the APS Division of Plasma Physics (Virtual, 9–13 November 2020) (<https://www.aps.org/meetings/meeting.cfm?name=DPP20>)